國 立 交 通 大 學

機 械 工 程 學 系

博士論文

電鍍鎳-鑽奈米複合材料之熱膨脹係數及疲勞特性研究

Investigation on Coefficient of Thermal Expansion and Fatigue Properties of Electroplated Ni-diamond Nanocomposite

研 究 生：黃家聖

指導教授：徐文祥、鄭裕庭

中華民國 九十八 年 十 月

電鍍鎳-鑽奈米複合材料之熱膨脹係數及疲勞特性研究

Investigation on Coefficient of Thermal Expansion and Fatigue Properties of Electroplated Ni-diamond Nanocomposite

研 究 生：黃家聖　　Student: Chia-Sheng Huang

指導教授：徐文祥　　Advisors: Wensyang Hsu

鄭裕庭　　Yu-Ting Cheng

國 立 交 通 大 學

機 械 工 程 學 系

博 士 論 文

A Dissertation

Submitted to Department of Mechanical Engineering

College of Engineering

National Chiao Tung University

in partial Fulfillment of the Requirements

for the Degree of

PhD

in

Mechanical Engineering

October 2009

Hsinchu, Taiwan

中華民國 九十八 年 十 月

電鍍鎳-鑽奈米複合材料之熱膨脹係數及疲勞特性研究

學生：黃家聖　　指導教授：徐文祥

鄭裕庭

國立交通大學機械工程學系 博士班

摘 要

電鍍鎳是微機電系統裝置中，常見的結構材料。近來更因為奈米科技的發展，結合奈米顆粒形成複合材料，不但強化了原先材料的特性，也增廣了電鍍鎳的應用範圍。在本論文中，將針對電鍍鎳-鑽奈米複合材料，於其熱膨脹係數變化機制、材料應用、材料可靠度議題等方面，做一完整的探討與研究。

於熱膨脹係數變化機制方面：利用文獻和 X 光繞射實驗的相互比對下，電鍍鎳基奈米複合材料內的殘留應力類型，可以藉由 X 光繞射角之峰值變化定義之，且被認定為最有可能影響奈米複合材料之熱膨脹係數變化的因素。而且此一來自製程的殘留應力，其類型可以由鎳基材與添加顆粒間的硬度差異或楊氏係數差異驗證之。根據實驗量測結果，電鍍鎳基材結合奈米鑽石顆粒，所形成的奈米複合材料呈現殘留壓應力，其熱膨脹係數可由原先電鍍鎳的 23 $\times 10^{-6}$/°C 提升至 50.1 $\times 10^{-6}$/°C；相對地，當電鍍鎳基材結合奈米二氧化矽顆粒，所形成的奈米複合材料則呈現殘留張應力，其熱膨脹係數由原先電鍍鎳的 23 $\times 10^{-6}$/°C 減少至 18 $\times 10^{-6}$/°C。

於材料應用方面：利用雙層板效應，電鍍鎳-鑽奈米複合材料的熱膨脹係數特性已被應用於一新型的鎳基熱雙層結構上。當熱雙層結構由電鍍鎳和電鍍鎳-鑽奈米複合材料疊合而成時，藉由電鍍鎳和電鍍鎳-鑽奈米複合材料兩者電鍍順序的調換，即可簡單地製作出向上或向下致動的熱雙層結構。加上這兩層鎳基材料具有相似的晶格結構的和相同的電鍍沈積溫度，其所製成的熱雙層結構，由實驗測試結果可知，擁有較佳的界面結合力和較低的熱殘留熱應力。

於材料可靠度議題方面：利用微機電製程與電鍍技術，分別製作電鍍鎳和電鍍鎳-鑽奈米複合材料的微懸臂樑測試試片，藉由出平面彎曲測試的方法，討論電鍍鎳與電鍍鎳-鑽奈米複合材料的疲勞特性與楊氏係數特性。根據實驗量測結果得知，由於奈米顆粒的添加，使得材料的延性降低，造成複合材料的疲勞強度略低於鎳基材；然而，當所添加的奈米顆粒尺寸由 350 nm 降至 50 nm 時，顆粒的尺寸效應則可使電鍍鎳-鑽奈米複合材料有~13.6%的楊氏係數提升，且具有與電鍍鎳可相比較的疲勞強度 (~2.4 GPa)。

Investigation on Coefficient of Thermal Expansion and Fatigue Properties of Electroplated Ni-diamond Nanocomposite

Student: Chia-Sheng Huang

Advisors: Wensyang Hsu
Yu-Ting Cheng

Department of Mechanical Engineering
National Chiao Tung University

Abstract

Electroplated Ni is the common structure material in MEMS devices. Recently, the nanotechnology has advanced it for enhanced material properties and wide applications by incorporated nano-particles. In this dissertation, the electroplated Ni-diamond nanocomposite has been investigated thoroughly in terms of CTE variation mechanism, material application, and reliability issue.

For the CTE variation mechanism, through the XRD investigation, residual stress types of Ni-based nanocomposites can be determined. These residual stresses resulted from co-deposited process are thought as the promising factor to affect the CTE variations. According to measurement results, the incorporated nano-diamond particles in Ni matrix will enhance the CTE of electroplated Ni from 23 to 50.1 $\times 10^{-6}$/°C with residual compressive stress; oppositely, the incorporated nano-SiO_2 particles in Ni matrix will diminish the CTE of electroplated Ni from 23 to 18 $\times 10^{-6}$/°C with residual tensile stress.

For the material application, the CTE property of Ni-diamond nanocomposite is applied on a newly Ni-based thermal bimaterial structure by bimorph effect. Thermal bimaterial structure made of electroplated Ni/Ni-diamond nanocomposite can achieve upward and downward out-of-plane displacement easily by controlling the plating sequence of electroplated Ni and Ni-diamond nanocomposite. Since Ni and Ni-diamond nanocomposite have different CTE but similar crystal structure and process temperature, the fabricated thermal bimaterial structures show better interfacial bonding strength and smaller residual thermal stress.

For the reliability issue, the characterizations of fatigue and Young's modulus have been studied employing the bending-test method on the specimens made of electroplated Ni and Ni-diamond nanocomposites. According to the measurement results, Ni-diamond nanocomposite has slightly smaller fatigue strength than that of pure electroplated Ni due to the ductility reduction resulted by the nanoparticles. However, once the particle size of nano-diamond is reduced from 350 to 50 nm, it has been found that the electroplated Ni-diamond nanocomposite can have higher Young's modulus (~13.6% enhancement) and comparable fatigue strength (~2.4 GPa) with that of pure electroplated Ni.

誌　謝

讀博士班就像跑馬拉松一樣，在孤寂的喘息聲中，一步步地考驗著自我的耐力與毅力。在這漫長的路程，最值得感謝的是沿途的啦啦隊、補給站以及加油的人群，讓我隨時能補充體力與活力跑完全程。所以這份榮耀，並不單單屬於我自己。在此，我希望藉由以下文字分享此份榮耀，衷心地紀錄和感謝一路上曾幫助我、關心我的朋友與家人。

首先，我要感謝我的指導教授：徐文祥老師。沒有他的知遇之恩，就沒今日的我。從碩士班到博士班這七年多的時間，老師除了提供無虞匱乏的實驗資源外，更盡心竭力地在研究上給予指導。而老師對於事物的剖析與獨特的見解，總令我印象深刻，我多麼希望時間可以暫停，好讓我能從他身上多挖一些寶石，以做為未來人生歷鍊的基石。

同時，我要感謝我的另一位指導教授：鄭裕庭老師。積極、有衝勁的他，在研究方法與論文撰寫方面的專業與態度，令我沒齒難忘也獲益良多。對我來說，老師就像生命中的貴人一樣，每當我的研究山重水複疑無路之時，他總是能適時、關鍵地指引我柳暗花明又一村。

其次，我要感謝清大材料黃振昌老師、師大機電楊啟榮老師、逢甲機電劉顯光老師，以及交大機械徐瑞坤老師、周長彬老師，在百忙之中願意擔任我博士論文的口試委員，並提供我許多研究上的寶貴意見。藉由口試的問答，老師們給了我許多不同觀點的想法，也讓我思考到許多沒注意到的問題。雖然口試時間短暫，但卻讓我獲益匪淺。

再次感謝徐文祥老師，因為有他，所以在這時空，我才能有這福氣和許多的實驗室夥伴相遇、共事。也因為有這些實驗室夥伴當後盾，我才能堅穩地跨出每一步。在這些實驗室夥伴中，感謝鍾君煒學長、楊涵評學長、邱雅惠學姐、蔡梨暖學姐、林郁欣學長、張駿偉學長、李毅家學弟、黃元德學弟、葉昌旗學弟，在專業知識上的解惑，

與實驗研究上的幫助。感謝葉昶志學弟與逢甲機電林瑜婷學妹的情義相挺，颱風夜仍堅守崗位，無怨無悔地幫我完成疲勞實驗，真的很感恩。感謝林軒宇學弟、胡皓宇學弟、蔣鎧宇學弟、廖淳旭學弟、王澤瑋學弟、吳松岳學弟、黃正鄴學弟，有了這些嗨咖學弟，實驗室總是充滿歡樂與活力，和他們相處的日子是我最快樂的時光。感謝鄭裕庭老師實驗室的陳永昌學弟與范士岡老師實驗室的許耀文學弟，和我一起作伴去美國參加會議、瘋狂購物，也一起吃到難吃的牛排。

這研究能完成，還要感謝交大奈米中心、國家奈米元件實驗室、國家晶片系統設計中心、國家儀器科技研究中心、勤益科大潘吉祥老師、逢甲機電劉顯光老師，提供代工服務、製程與量測設備。

最後，我要衷心地感謝養育我的銀河爸爸和月卿媽媽，謝謝家芯妹妹和家鴻弟弟，謝謝月華阿姨、月霞阿姨、劉傳姨丈，感謝你們的支持與關心、加油與鼓勵。還有最重要的是，感謝瓊慧能耐心地陪我走過這段艱辛的日子，謝謝妳為我所承受及付出的一切。

～ 謹以本論文，獻給一路上曾幫助我和關心我的朋友與家人。謝謝你們，感恩。 ～

家聖 于 新竹・交大

2009/10/10

Content

List of Tables

List of Figures

Chapter 1 Introduction

1.1 Motivation

Electro-deposition technique is a cost-effective fabrication with high integration of microelectro-mechanical systems (MEMS). This technique provides several advantages including flexible material choice (ex. Cu, Ni, Cr, Zn, Cd, Sn, Ag, Au, etc), low temperature compatible process of complementary metal-oxide-semiconductor (CMOS), and high manufacturing throughput. Electroplated nickel (Ni) is a common structure material in MEMS devices, because it has low electrical and thermal resistivity (for conduct structure), low processing temperature (~50 °C, for post-fabrication), high Young's modulus (for robust structure), and high deposition rate (for thicker structure and higher throughput). During last decades, lots of research works have been done in the electroplated Ni for MEMS applications [1-6]. Zavarcky et al. [3] developed a surface micromachining process of electroplated Ni to fabricate micromechanical switches to demonstrate the integrated feasibility of post-process and conventional circuit due to the lack of high temperature steps in the electroplating process. Hsu et al. [4] proposed a Ni-based large-stretch micro drive (LSMD) of electro-thermal microactuator for generating large output displacements (~280 μm) with low operating voltages (~0.5 V). Kataoka et al. [5] presented a MEMS probe card made of electroplated Ni microcantilevers for lower contact resistances between Ni probe and Al electrodes. Huang et al. [6] demonstrated the integration of Ni-based monolithic oscillator with CMOS circuitry via MEMS-last (or called post-CMOS MEMS) technology.

Recently, nanotechnology has advanced the electro-deposition technique for high performance MEMS fabrication in terms of material property enhancement by nanocomposite effect [7]. More and more investigations in the nanocomposite syntheses

and characterizations show that the intrinsic physical property limits of metal, including wear resistance, hardness, Young's modulus, and coefficient of thermal expansion (CTE), can be further modified and strengthened via the incorporation of well dispersed nanoparticles like SiC, Al_2O_3, Si_3N_4, diamond, etc [8-14]. Thus, for MEMS fabrication, employing the nanocomposite synthesized by electro-deposition process has revealed its excellent prospect.

Previously, our groups had shown that adding nano-diamond particles into Ni plating to form the electroplated Ni-diamond nanocomposite can have modified Young's modulus, hardness, and CTE comparing with the pure electroplated Ni. Tsai et al. [12, 13] found that the electro-thermal microactuator made of Ni-diamond can save 73% power consumption comparing with the one made of pure electroplated Ni for the same output displacement via CTE enlargement of structural material. Lee et al. [14] demonstrated micro-resonator made of Ni-diamond nanocomposite could have higher resonance frequency than the one made of pure electroplated Ni via Young's modulus improvement of structural material, which could be helpful in RF-MEMS application. Therefore, the electroplated Ni-diamond nanocomposite has been thought as a potential structure material for further applications of micromachines and MEMS devices.

It is well known that mechanical properties of thin films are different from those of bulk materials. This difference can be explained by the large surface-volume ratio, since the microstructure of the surface will have significant influence on the mechanical properties of thin film [15]. Therefore, information on the mechanical properties of constructed materials has become essential for the further designs and applications of micromachines and MEMS devices. Furthermore, in order to achieve the long-term reliability in various micromachines and MEMS devices, especially for micro-components under cyclic motion, it is necessary to understand the mechanical properties of constructed

materials including fracture, fatigue, elastic, plastic, etc. Up to now, however, related mechanical properties of electroplated Ni-diamond nanocomposites and long-term reliability of the composite devices have not been well studied and examined.

In this dissertation, a fatigue characterization scheme based on the bending-test design will be proposed and utilized for the investigations of mechanical property and reliability issue on the Ni-diamond nanocomposites, which are incorporated with different particle sizes (i.e. 350 nm and 50 nm in diameter), in terms of Young's modulus, fatigue lifetime, fatigue strength, and fracture mechanism. Furthermore, in the previous investigation [12, 13], the reason of CTE enhancement on the pure electroplated Ni by incorporated nano-diamond particles is not clear yet and needs to be further studied. Here, through past literatures and X-ray diffraction (XRD) investigation on electroplated Ni-based nanocomposites with different nano-particle types (i.e. diamond and SiO_2), the promising factor will be proposed to explain the CTE variation mechanism in the Ni-based nanocomposite. Subsequently, this CTE property will be applied on a newly Ni-based thermal bimaterial structure by bimorph effect.

1.2 Background

1.2.1 Electroplated Ni-diamond Nanocomposite

Metal matrix composites (MMCs) are composed of a metal matrix and a reinforcement, which confers excellent mechanical performance, and can be classified according to whether the reinforcement is continuous (monofilament or multifilament) or discontinuous (particle, whisker, short fiber or other) [16]. For the electroplated Ni-diamond nanocomposite, the consisted materials of metal matrix and reinforcement are electrodeposited Ni and dispersed nano-diamond particles, respectively. Through the mechanism of co-deposition, the electroplated Ni-diamond nanocomposite was fabricated

for expected material properties including electrical and wear resistance, hardness, Young's modulus, and CTE. Figure 1.1 shows the mechanism of particles co-deposition into growing metallic layers [7]. Five consecutive steps during the co-deposition process can be identified: (1) formation of ionic clouds on the particles, (2) convection towards the cathode, (3) diffusion through a hydrodynamic boundary layer, (4) diffusion through a concentration boundary layer and finally, (5) adsorption at the cathode where particles are entrapped within the metal deposit.

In 1983, Zahavi and Hazan [17] firstly characterized the relationship of concentration and particle size (0.5 ~ 40 μm natural and synthetic diamonds) in Ni-diamond coatings and discuss structure, morphology and wear resistance. They found that the particle concentration of either nature or synthetic diamond particles increased with decrease current density and agitation intensity. The wear resistance of the coating increased with an increase in particle size, giving maximum wear resistance with 3 ~ 6 μm diamond particles.

In 1999, Lee et al. [18] used the direct current (DC) and pulse plating methods to codeposited Ni and nanometer-diamond powder (average size of 25 nm) on Cu substrate to discuss the effect of diamond concentration, current density, current frequency, plating temperature, plating time, and stirring speed on microhardness and friction coefficient of codeposited layer. They found that a plating temperature ranging from 30 to 50 °C and a stirring speed below 300 rpm were suitable for the Ni-diamond co-deposition. With the increasing diamond concentration, the microhardness and surface roughness of the codeposited layer were increased. The microhardness of Ni-diamond made by pulse-plating method was 13% enhancement than that made by DC plating method.

In 2001, Lee and Choi [19] investigated the co-deposition behavior of diamond particles (2 ~ 30 μm sized artificial diamond particles) and Ni onto a steel in Ni sulfamate

baths by using both a rotating disc and wire geometries. They found that since the rate of Ni deposition was controlled by both mass transfer of the Ni ions and electrochemical deposition, the diamond content in Ni-diamond deposition decreased with increasing applied potential and stirring speed in the relatively high rotation speed ranges.

In 2005, unlike previous researches on the optimization between plating condition and diamond concentration, Teh et al. [20] showed the possible application of Ni-based composite on MEMS device, and demonstrated it as a potential structural material due to the advantages of low-temperature, stress-free, and wafer-level fabrication. They found that the incorporation of nano-diamonds (diameter ~4 nm) in electrolytic Ni matrix to form Ni-diamond nanocomposite could reduce the film residual stress and render the film more compressively.

In 2006, our groups, Tsai et al. [12] and Lee et al. [14] successfully demonstrated the applications of Ni-diamond nanocomposites on MEMS devices including electro-thermal microactuator and electrostatic comb-drive, respectively. They found that adding nano-diamond particles (diamond diameter <0.5 μm) into nickel plating to fabricate Ni-diamond nanocomposite could enhance not only the Young's modulus but also the CTE than that of pure electroplated Ni.

From above reviews, we can find that the electroplated Ni-diamond nanocomposite is a potential material for MEMS applications. In material properties, electroplated Ni-diamond nanocomposite has advantages of well wear resistance, high hardness, high Young's modulus, high CTE, and stress-free than that of pure electroplated Ni. In fabrication processes, electroplated Ni-diamond nanocomposite, like pure electroplated Ni with MEMS and CMOS compatibility, has advantages of one-step process, selective on-chip deposition, high deposition rate, low process temperature, and wafer-level fabrication. Due to the further designs and applications of micromachines and MEMS

devices, especially for micro-components under cyclic motion, the reliability issue of electroplated Ni-diamond nanocomposite should be characterized.

1.2.2 Fatigue Test Methods

Fatigue is a form of failure that occurs in structures subjected to dynamic and fluctuating stresses. Under these conditions it is possible for failure to occur at a stress level considerably lower than the tensile or yield strength for static load. The term "fatigue" is used because this type of failure normally occurs after a lengthy period of repeated stress or strain cycling. Fatigue is important inasmuch as it is the single largest cause of failure in metals, estimated to comprise approximately 90% of all metallic failures; polymers and ceramics (except for glasses) are also susceptible to this type of failure. Furthermore, it is catastrophic and insidious, occurring very suddenly and without warning [21]. Therefore, the fatigue property of the structure material is an important criterion of device reliability. If we can know the fatigue property of the structural material in advance, the device lifetime can be predicted. That is helpful to design practical micromachines and MEMS devices because the moving components involved in these devices are subjected to cyclic loading.

In the conventional fatigue test of bulk materials, a rotating-bending test apparatus, commonly used for fatigue test, is shown in Figure 1.2; the compression and tensile stresses are imposed on the specimen as it is simultaneously bent and rotated [21]. Tests are also frequently conducted using an alternating uniaxial tension-compression stress cycle.

With the device miniaturization, the conventional fatigue test method is no longer suitable for micrometer-scale specimen. Considering the size, grip, alignment, and loading of specimen, a new fatigue test method is necessary including testing techniques,

specimen design, and equipment. However, there are no standard test methods so far. Among these test methods of approaches, tensile and bending tests are two common schemes for the fatigue characterization on micrometer-scale specimens. And the microsized cantilever-beam is utilized frequently in specimen design. As shown in Figure 1.3, according to loading methods on the free end of the cantilever-beam, three fatigue test types can be identified: (1) in-plan tensile method, (2) in-plane bending method, and (3) out-of-plane bending method.

For the in-plan tensile method, in 2003, Cho et al. [22] used microsample tensile machine and non-contact interferometer strain displacement gage to study the fatigue properties of electrodeposited LIGA Ni microsamples (~400 μm thick) with dog-bone shape under the test frequency of 200 Hz, as shown in Figure 1.4. The test results indicated that the fatigue lifetime of the LIGA Ni microsamples increased with decreasing stress amplitude, and the measured fatigue limit and endurance ratio were 195 MPa and 0.35, respectively. In 2004, Son et al. [23] evaluated and discussed the fatigue properties and notch effect of LIGA Ni film (10 μm thick) by micro-tensile and fatigue test methods under the test frequency of 20 Hz, as shown in Figure 1.5. The test results indicated that the fatigue strength of LIGA Ni was very sensitive to stress concentration, and the measured fatigue limit and endurance ratio were 180 MPa and 0.21 for unnotched specimens, and 143 MPa and 0.17 for notched specimens, respectively. In 2007, Yang et al. [24] also used the micro-tensile testing system to study the fatigue mechanisms of LIGA Ni thin films (70 μm and 270 μm thick) with micro-scale and nano-scale grains under the test frequency of 10 Hz, as shown in Figure 1.6. The test results indicated that films with the nano-scale grains (15 nm average grain size) were shown to have higher strength and fatigue resistance than those with micro-scale columnar grain structures (5 μm wide and 5 ~ 25 μm long). The thinner films (70 μm thick with a columnar microstructure) were also

shown to have higher strength and fatigue resistance than those of thicker films (270 μm thick with a columnar microstructure).

For the in-plan bending method, in 2003, Larsen et al. [15] proposed an in situ bending test device with integrated electrostatic actuator and test beam, made of electroplated nanocrystalline Ni (7 μm thick), for fatigue investigation under the test frequency of 200 Hz, as shown in Figure 1.7. The feature of this test device was approximately pure in-plane bending, and the maximum stresses were calculated using finite element method. The test results indicated that the nanocrystalline Ni had good fatigue properties due to the high strength and toughness of nanocrystalline material. However, the clear fatigue limit and endurance ratio were not obtained in this study.

For the out-of-plan bending method, in 1999, Maekawa [25] et al. performed fatigue lifetime and fatigue crack propagation tests on electroless plated Ni-P amorphous alloy specimen (12 μm thick) to investigate the material fatigue properties under the test frequency of 10 Hz, as shown in Figure 1.8. The microsized specimens were cantilever-beam-type prepared by focused ion beam (FIB) machining, and notches with a depth of 3 μm were introduced in some specimens. The fatigue lifetime curve was obtained for unnotched specimens, and the fatigue crack propagation tests were performed using notched specimens. The test results indicated that the crack was deduced to propagate by cyclic plastic deformation at the crack tip even in microsized amorphous alloys, and the measured fatigue limit and endurance ratio were 20 mN and 0.43, respectively.

From above reviews, we can find that once the sample becomes very small only with several micrometers, the setup of tensile method become stringent to grip, align, and pull a tested sample. In comparison with the tensile method, the bending method can be free of the issues raised by sample gripping and alignment. Furthermore, bending method

requires smaller loading force than that of tensile tests to yield a tested sample with a deformation that is large enough for accurate measurement, which makes the method suitable for thin film characterization. Thus, in this dissertation, a fatigue characterization scheme based on the design of out-of-plane bending method is proposed and utilized for the property investigations on the electroplated Ni and Ni-diamond nanocomposite.

1.3 Dissertation Outline

The goal of this dissertation is to investigate CTE and fatigue properties of electroplated Ni and Ni-diamond nanocomposite in terms of CTE variation mechanism, material application, and reliability issue. The detailed study including fabrication and measurement methods, experimental results, and characterizations are described in the following chapters.

In Chapter 2, the promising factor is proposed to explain the CTE variation by using the XRD investigation on electroplated Ni-based nanocomposites with different nano-particle types (i.e. diamond and SiO_2).

In Chapter 3, the application of CTE property on bimorph effect is investigated by Ni/Ni-diamond nanocomposite, and a newly Ni-based thermal bimaterial structure for sensor and actuator application is also proposed.

In Chapter 4, a fatigue characterization scheme based on the bending-test design is proposed and utilized for the property investigations on the electroplated Ni and Ni-diamond nanocomposite (incorporated with two different particle sizes, i.e. 350 nm and 50 nm in diameter) in terms of Young's modulus, fatigue lifetime, fatigue strength, and fracture mechanism.

Finally, Chapter 5 concludes this dissertation and suggests the future research direction.

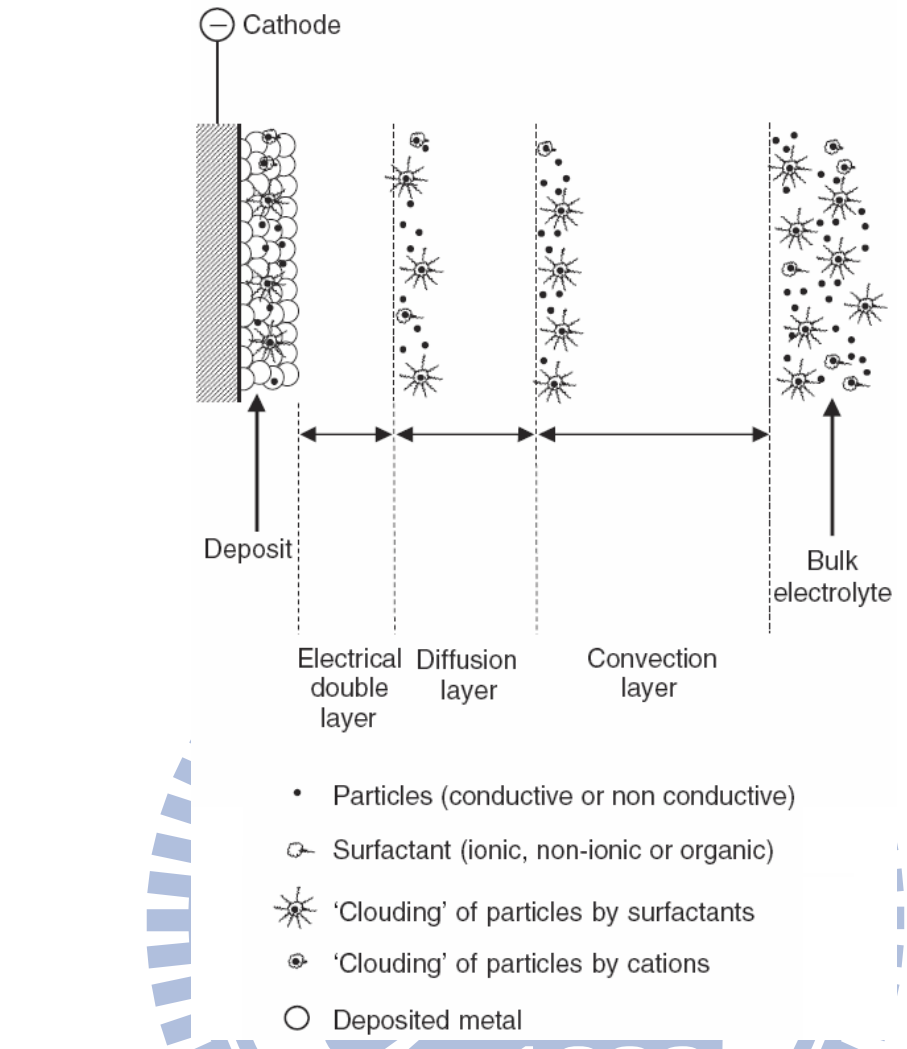

Figure 1.1 Mechanism of particles co-deposition into a metal deposit. [7]

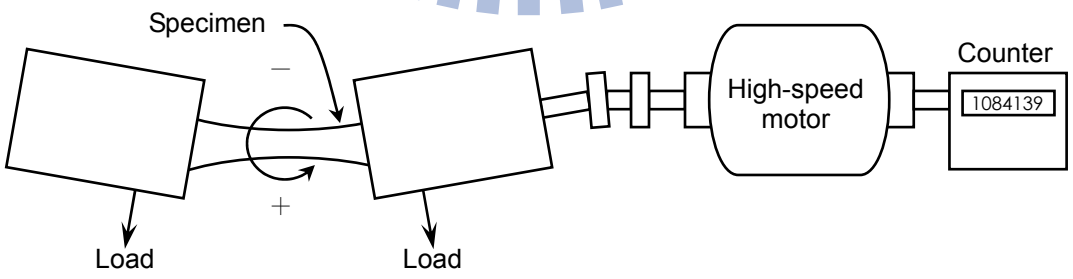

Figure 1.2 Fatigue test apparatus for making rotating-bending test. [21]

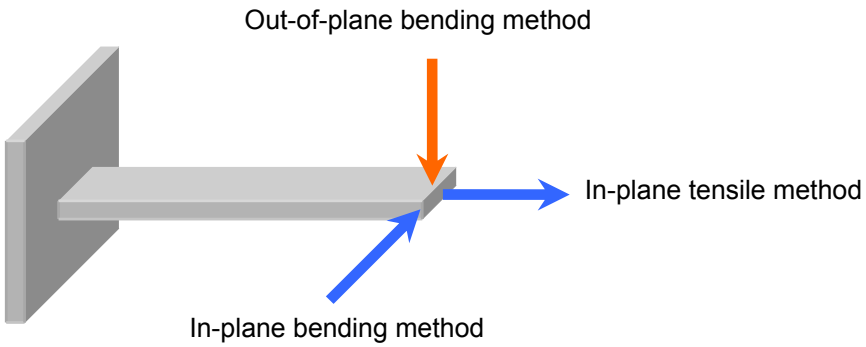

Figure 1.3 Common fatigue test types classified by loading methods.

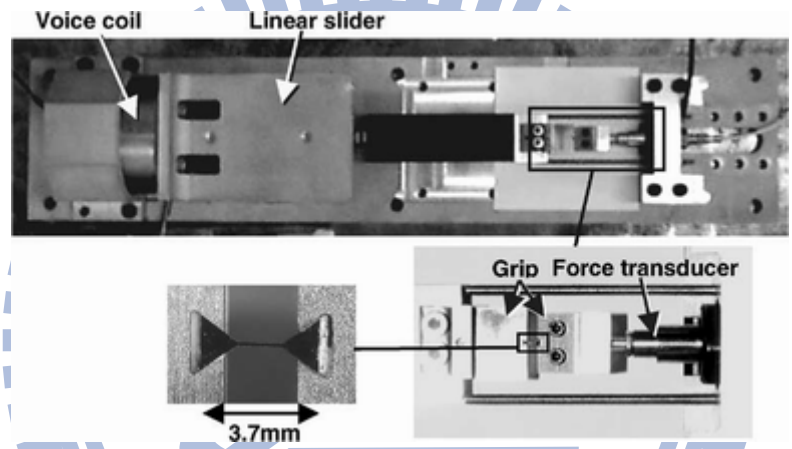

Figure 1.4 In-plan tensile method of fatigue test: test machine and specimen. [22]

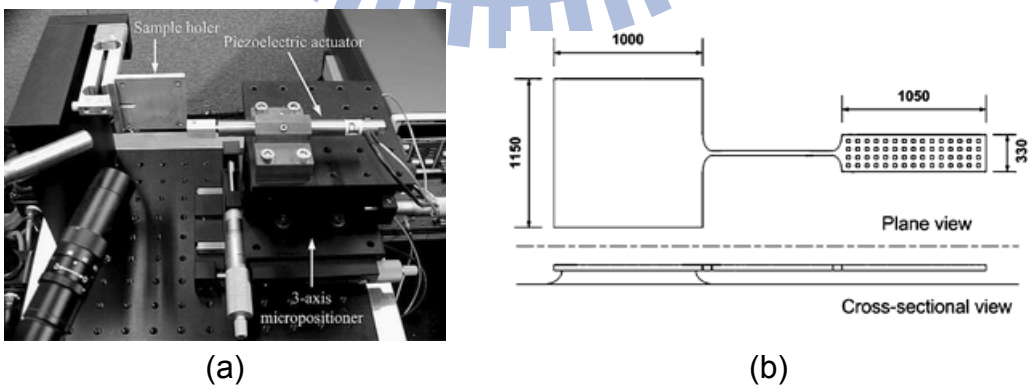

Figure 1.5 In-plan tensile method of fatigue test: (a) test system, and (b) schematic diagram of specimen. [23]

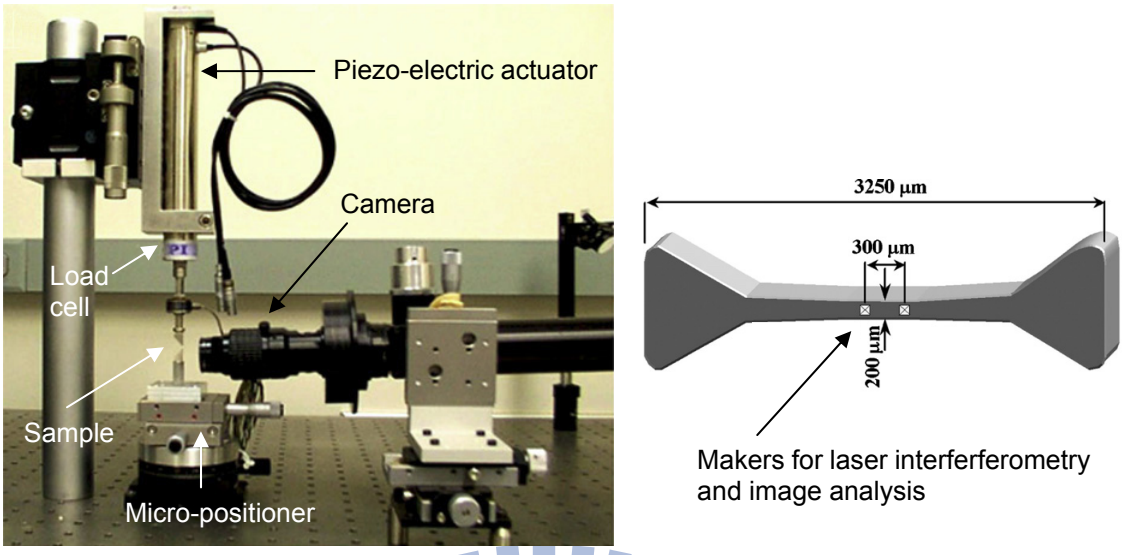

Figure 1.6 In-plan tensile method of fatigue test: (a) test system, and (b) schematic dog-bone shape sample. [24]

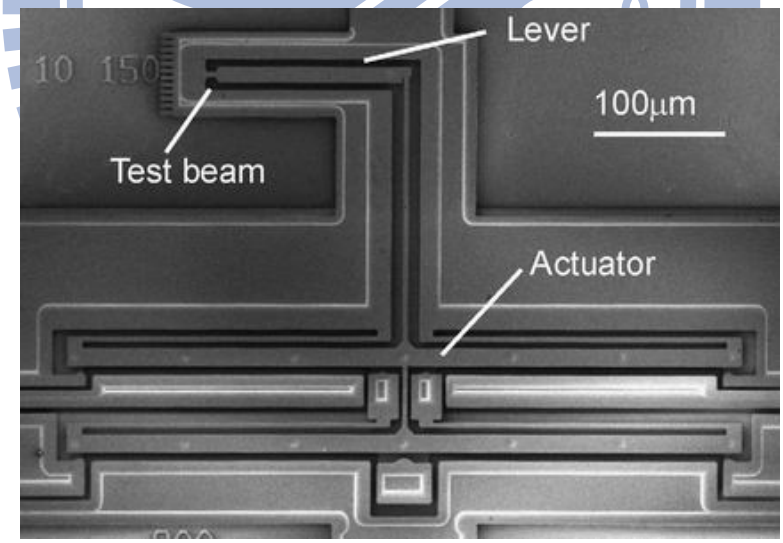

Figure 1.7 In-plan bending method of fatigue test: fatigue test device integrated with test beam and electrostatic actuator. [15]

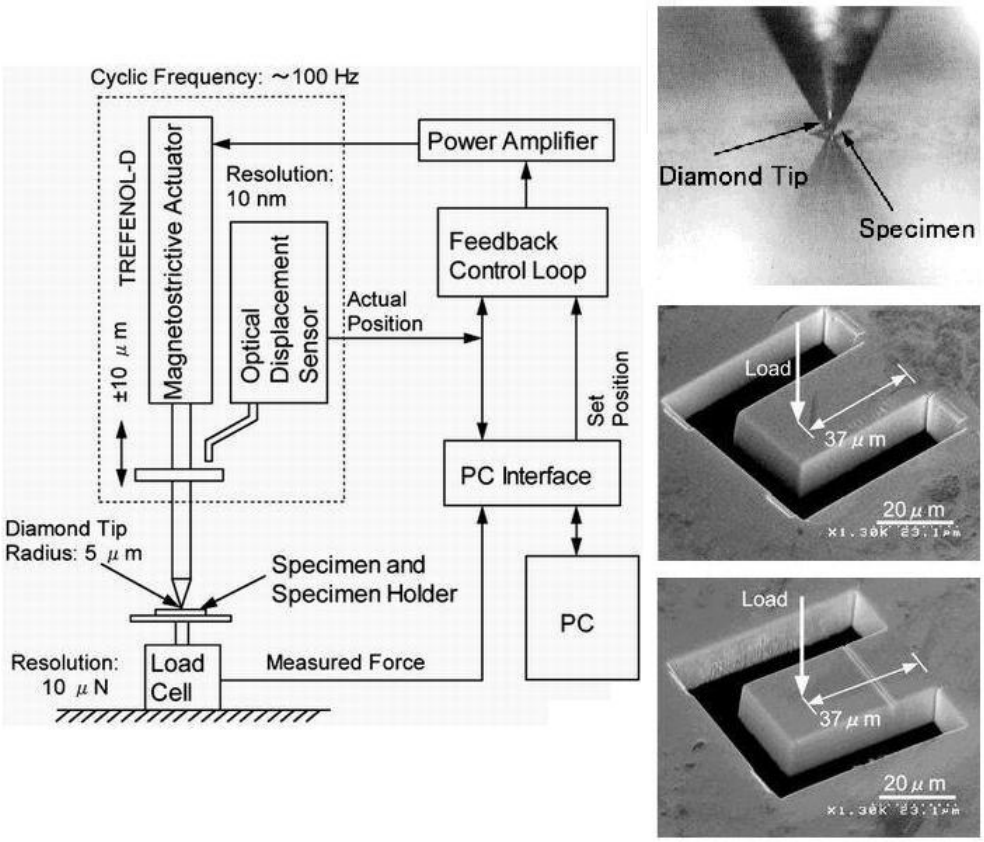

Figure 1.8 Out-of-plan bending method of fatigue test: block diagram of test system and microsized specimens without/with notch. [25]

Chapter 2 Investigation on CTE Property

2.1 Introduction

In the previous investigation, our group, Tsai et al. [12, 13] found that the electro-thermal microactuator made of Ni-diamond can reduce 73% power requirement comparing with the electroplated Ni one for the same output displacement of 3 μm, and can enlarge the reversible displacement range from 1.8 μm to 3 μm (i.e. more than 67% ultimate elongation), simultaneously. These performance enhancements were resulted by the augment of CTE of Ni via the nano-diamond particles incorporation. However, such a CTE enhancement does not follow the rule of mixtures (ROMs) in metal matrix composites (MMCs). There must be some factor that affects the CTE variation via the incorporated nano-diamond particles in the Ni-diamond nanocomposite.

In this study, referring to the past literatures and employing the XRD investigation, the promising factor is proposed to explain the CTE variation on electroplated Ni-based nanocomposites with different nano-particle types (i.e. diamond and SiO_2).

2.1.1 Rule of Mixtures

ROMs are the common function to predict the CTE of MMCs. In general, the CTE of MMCs is usually assumed to follow a simple ROMs dependence on volume fractions of presence phases, known as the linear ROMs [26, 27]:

$$\alpha_c = V_m \alpha_m + V_p \alpha_p \tag{2.1}$$

where α is the CTE and V is the volume fraction. The subscripts of c, m, and p denote composite, matrix phase, and particle phase, respectively. In fact, the CTE of MMCs is hard to be predicted only using the linear ROMs because it is affected by several factors such as reinforcement volume fraction, fabrication process, and the nature of the

composite constituents [28]. For the linear ROMs, it assumes the composite is a simple mixture of two phases with each phase exhibiting physical behaviors that are not influenced by their presence in mixture, and therefore the effects of microstructure, plasticity, and thermal softening are not account for. To improve the accuracy of the linear ROMs, several models have been proposed for predicting the CTE of MMCs. Among these, the most often mentioned and used are Turner [29], Kerner [30], and Schapery [31] models. To begin with the Turner's model, it assumes homogeneous strain throughout the composite and uses a balance of internal average stresses. By considering that the sum of the internal forces equals to zero, the CTE of MMC is obtained:

$$\alpha_c = \frac{\alpha_p V_p K_p + \alpha_m V_m K_m}{V_p K_p + V_m K_m} \tag{2.2}$$

where K is the bulk modulus which calculated using the standard relationship of Young's modulus (E) and Poisson's ratio (υ): $K = E/3(1-2\upsilon)$. Next, the Kerner's model assumes that the particle is spherical and clothed by a uniform layer of matrix. By considering that the composite is the volume element, the CTE of MMC becomes:

$$\alpha_c = \overline{\alpha} + \frac{V_p(1-V_p)(\alpha_p - \alpha_m)(K_p - K_m)}{(1-V_p)K_m + V_p K_p + (3K_p K_m / 4G_m)} \tag{2.3}$$

where $\overline{\alpha}$ is the linear ROMs CTE as expressed in Equation 2.1 and G is the shear modulus which calculated using the standard relationship of Young's modulus and Poisson's ratio: $G = E/2(1+\upsilon)$. Lastly, the Schapery's model has been developed by considering the thermoelasticity based on extremum principles for predicting the CTE of isotropic composites. The CTE of MMCs can be expressed as the following equation:

$$\alpha_c = \alpha_p + (\alpha_m - \alpha_p)\left[\frac{1/K_c - 1/K_p}{1/K_m - 1/K_p}\right] \tag{2.4}$$

where the K_c is the bulk modulus of composite [28, 32]. In this study, the related values

of α, E, and υ used for computing the predicted CTE of Ni-diamond nanocomposite by Equations 2.1 ~ 2.4 are extracted from previous experiment work [12, 13, 21, 33] that the Young's modulus of pure electroplated Ni is measured by means of a nanoindentation test, the CTE value of Ni-based nanocomposite is measured by calculating the elongation-temperature ratio of Ni-based microcantilever beam during the temperature range from room temperature (~25 °C) to 400 °C, and the weight fraction of diamond in nanocomposite is measured by the elemental analyzer (EA). As shown in Figure 2.1, the computing results of the predicted CTE of Ni-diamond nanocomposite using Equations 2.1 ~ 2.4 are plotted.

Figure 2.1, compares the CTE values of Ni-diamond nanocomposites between experimentally measured data and theoretically predicted calculations in the range of 0% ~ 2% volume fraction of diamond. It shows that the experimental CTE values of Ni-diamond nanocomposites, which don't follow the theoretical ROMs, are higher than that of theoretical predictions and the matrix material of pure electroplated Ni (23 $\times 10^{-6}$/°C, as measured). Furthermore, the experimental CTE values of Ni-diamond nanocomposites increase with the volume fraction and the particle size of nano-diamond. For the nanocomposites plated in a bath with an average diameter of 350 nm nano-diamonds, the CTE values increase from 31.5 $\times 10^{-6}$/°C to 50.1 $\times 10^{-6}$/°C while the volume fraction increase from 0.19% to 0.47%. With the size enlargement of nano-diamond particles, the CTE values are found to increase from 38.0 $\times 10^{-6}$/°C of the composite synthesized with an average diameter of 50 nm nano-diamonds up to 50.1 $\times 10^{-6}$/°C of that with an average diameter of 350 nm nano-diamonds.

2.1.2 Particle Effect

In order to investigate the particle effect on CTE of Ni-based nanocomposite [13], electroplated Ni-SiO_2 nanocomposite is prepared by adding SiO_2 nanoparticles with an average diameter of 80 nm into Ni plating bath. As shown in Table 2.1, the plating conditions of pH values and temperatures are maintained at 4.1 ~ 4.3 and 50 °C, and the concentration of the SiO_2 nanoparticles are ranging from 0 g/L to 0.036 g/L which are determined by the same volume fraction of nanoparticles inside Ni plating bath as nano-diamonds. In Figure 2.2, the measured CTE values of Ni-SiO_2 nanocomposites with different particle concentration are obtained by calculating the elongation-temperature ratio of Ni-SiO_2 microcantilever beams during the temperature range from room temperature to 400 °C. The measured results show that the added SiO_2 nanoparticles will diminish the CTE values of electroplated composites, and the nanocomposite of Ni-SiO_2 has opposite CTE performance from Ni-diamond. In our experiment results of Ni-SiO_2 nanocomposites, the CTE values are found to decrease from 22 $\times 10^{-6}$/°C to 18 $\times 10^{-6}$/°C with the augment of SiO_2 nanoparticles concentration in plating bath from 0.008 g/L to 0.036 g/L.

From the preliminary investigation of particle effect, up to now, the CTE enhancements of Ni are attributed to the incorporation of nano-diamond particles. As mentioned before, however, such a CTE enhancement can't be explained by the ROMs of MMCs in Equations 2.1 ~ 2.4. There must be some factors, which affect CTE property of Ni-diamond nanocomposite, needing further investigation.

2.1.3 Factors that Affect CTE

From the literature survey, the related research of CTE enhancement is limited and only can be found in pure material. In these limited researches, the factors that affect

CTE enhancement can be attributed to crystalline grain size [34, 35] and stress modes including microstress (ex. microstrain [36]) and macrostress (ex. pre-stressing [37, 38] and residual stress [39]).

For the factor of crystalline grain size, in 1989, Birringer [34] found that the CTE of nanocrystalline Cu (grain size ~8 nm) was about 1.94 times than that of conventional polycrystalline counterpart. In 1995, Lu and Sui [35] found that the CTE of porosity-free nanocrystalline Ni-P (grain size <127 nm) increased with the reduction of crystalline grain size.

For the factor of microstress, in 2002, Qian et al. [36] found that the CTE of nanocrystalline Cu increased by about 12% with an increment of the microstrain from 0.14% to 0.24% which was conducted by quantitative XRD measurements. In addition, the microstrain effect on thermal properties in the nanocrystalline Cu might be attributed to the change in density of grain boundary defects/dislocations.

For the factor of macrostress in pre-stressing, in 1970, Gazda [37] found that a compressive pre-stressing caused the CTE of graphite to increase and that annealing caused the CTE to decrease toward the original value. As expected, the 90% compression samples gave the largest changes in CTE. It was also interesting to note that the increase in CTE appeared to be independent of particle size, but dependent on the grain orientation. In addition, the CTE resulted in the direction perpendicular to the compression gave very slight CTE increase. In 1971, Hart [38] found that uniaxial compressive loading resulted in an increase in CTE of graphite, but tensile loading caused an opposite effect. This result can be explained by the crack closure model [40] which is used to explain graphite thermal expansion accommodation. In the present work, uniaxial compression caused an increase in specimen density and a corresponding increase in thermal expansion. This suggested that cracks which initially contributed to accommodation were closed under

compressive loading modes. On the other hand, tensile pre-stressing reduced density (i.e. opened additional cracks) and reduced thermal expansion. In addition, this research was also shown that all loading mode caused a decrease in the Young's modulus due to the increased dislocation density and cracking induced by pre-stressing.

For the factor of macrostress in residual stress, in 2000, Fang and Lo [39] found that the CTE of the Al thin film increased from 18.23 $\times 10^{-6}$/°C to 29.97 $\times 10^{-6}$/°C as the film thickness increased from 0.3 μm to 1.7 μm under residual compressive stress. Oppositely, the CTE of the Ti thin film decreased from 21.21 $\times 10^{-6}$/°C to 9.04 $\times 10^{-6}$/°C as the film thickness increased from 0.1 μm to 0.3 μm under residual tensile stress.

From above researches, in order to further discuss the effects of crystalline grain size and stress mode on the CTE property of Ni-based nanocomposite, the following XRD investigation will be performed.

2.2 Measurements and Discussions

2.2.1 Grain Size Measurement

As shown in Figure 2.3, the XRD patterns of as-fabricated pure Ni, Ni-diamond (average particle size: 350 nm; particle concentration: 2 g/L), and Ni-SiO_2 (average particle size: 80 nm; particle concentration: 0.036 g/L) nanocomposites are measured by the X-ray diffractometer (PANalytical X'Pert Pro MRD) using $\theta - 2\theta$ scan with Cu-Kα radiation (i.e. wave length λ=1.5405 Å). In Figure 2.3, the face-centered-cubic (FCC) texture of electroplated pure Ni, Ni-diamond, and Ni-SiO_2 nanocomposites have been observed with the preferred orientation of (111). Therefore, in this study, the diffraction peak (111) is chosen for the calculation of crystalline grain size, and the crystalline grain size is estimated according to the Scherrer's formula [41]:

$$D = \frac{0.9\lambda}{\beta \cos\theta} \tag{2.5}$$

where λ is the wave length, β is the full width at half maximum (FWHM), and θ is the diffraction angle which is half of the peak centroid.

By the commercial analysis software (MDI Jade 5.0), the related parameters of Equation 2.5 can be derived from the XRD data (i.e. Figure 2.3) as shown in Table 2.2. The calculated results show that the crystalline grain sizes of electroplated Ni, Ni-diamond, and Ni-SiO_2 nanocomposites are 20.5 nm, 20.0 nm, and 21.6 nm, respectively. It is noted that these grain sizes are similar to each other in nanometer size. There is no dramatically size variation from micro-scale to nano-scale. Thus, the effect of crystalline grain size can be eliminated from the factors that affect CTE.

2.2.2 Stress Mode Investigation

For the investigation on stress mode, as shown in Figure 2.4, the measurement of microstrain (for microstress) and macrostrain (for macrostress) are performed by the XRD peak broadening and peak shift, respectively, which are based on Bragg's law as follows [41-44]:

$$\lambda = 2d \sin\theta \tag{2.6}$$

where λ is the wave length, d is the spacing of the diffraction plane, and θ is the diffraction angle. The microstrain is determined by the XRD peak broadening (i.e. the change of FWHM) as follows [41, 42]:

$$\varepsilon_{micro} = \frac{\Delta\beta}{4\tan\theta} \tag{2.7}$$

Comparing between Equation 2.5 and Equation 2.7, it can be found that the change of FWHM (β) depends on crystalline grain size (D). As mentioned before, thus, the effect of microstress can also be eliminated from the factors that affect CTE.

From Equation 2.6, it can be found that if an additional force yields a lattice spacing reduction (i.e. compressive strain), the position of XRD peak (i.e. diffraction angle) will

shift toward a higher angle On the contrary, the yielded expansion of lattice spacing (i.e. tensile strain) will cause peak position shift toward a lower angle. Therefore, the macrostrain can be determined by the XRD peak shift (i.e. the change of lattice spacing) as follows [41, 43, 44]:

$$\varepsilon_{macro} = \frac{d' - d_0}{d_0} = \frac{\Delta d}{d_0} \tag{2.8}$$

where d_0 is the lattice spacing of stress-free material and d' is the lattice spacing for strained material. From the Equation 2.6 and XRD data of Figure 2.3, the spacing values of electroplated Ni, Ni-diamond, and Ni-SiO_2 nanocomposites can be determined as shown in Table 2.2. Based on the pure electroplated Ni, the macrostrains of Ni-diamond and Ni-SiO_2 nanocomposites can be determined as -0.15% and 0.09%, respectively. It is noted that the incorporation of nano-diamond particles in Ni matrix causes compressive strain in nanocomposite, and the incorporation of SiO_2 nano-particles in Ni causes tensile strain in nanocomposite.

Combining with the experimental CTE data, Ni-diamond nanocomposite with compressive stress inside is observed to have higher CTE value than that of pure electroplated Ni. As opposed to Ni-diamond nanocomposite, Ni-SiO_2 nanocomposite with tensile stress inside is observed to have lower CTE value than that of pure electroplated Ni. Therefore, from the previous literature review, the factor of macrostress effect may be the main reason which causes the CTE variation on Ni-based nanocomposites.

In this dissertation, this stress difference between Ni-diamond and Ni-SiO_2 nanocomposites is though coming from the fabrication process, so-call residual stress, according to the hardness or Young's modulus difference between Ni matrix and nanoparticles. From the hardness and Young's modulus measurement of electroplated pure Ni, Ni-diamond, and Ni-SiO_2 nanocomposites [12, 13] as shown in Figures 2.5 and

2.6 respectively, it can be found that Ni matrix incorporated with higher hardness and Young's modulus of diamond particles conducts higher hardness and Young's modulus of Ni-diamond nanocomposite than that of electroplated pure Ni due to the simple rule of mixtures [21]. Oppositely, Ni matrix incorporated with lower hardness and Young's modulus of SiO_2 particles conducts lower hardness and Young's modulus of Ni-SiO_2 nanocomposite than that of electroplated pure Ni. Therefore, during co-electrodeposited process of Ni-diamond nanocomposite, diamond particles will construct a compressive stress to Ni matrix due to its higher hardness and Young's modulus than that of Ni matrix, as shown in Figure 2.7(a). On the contrary, for Ni-SiO_2 nanocomposite as shown in Figure 2.7(b), the hardness and Young's modulus of SiO_2 particles are lower than that of Ni matrix so that SiO_2 particles will construct a tensile stress to Ni matrix during co-electrodeposited process.

2.3 Summary

Through the XRD investigation on peak shift, residual stresses types of Ni-based nanocomposites compared with pure electroplated Ni can be determined. These residual stresses, which are constructed from co-electrodeposited process due to the hardness or Young's modulus difference between matrix and particles, are thought as the promising factor to affect the CTE variations in nanocomposites. For Ni-diamond nanocomposite, the measured result shows that the incorporated nano-diamond particles (average particle size: 350 nm; particle concentration: 2 g/L) will enhance the CTE of electroplated Ni from 23 $\times 10^{-6}$/°C to 50.1 $\times 10^{-6}$/°C with residual compressive stress (0.15% compressive strain). Oppositely, for Ni-SiO_2 nanocomposite, the measured result shows that the incorporated nano-SiO_2 particles (average particle size: 80 nm; particle concentration: 0.036 g/L) will diminish the CTE of electroplated Ni from 23 $\times 10^{-6}$/°C to 18 $\times 10^{-6}$/°C with residual tensile

stress (0.09% tensile strain). Therefore, employing a simple composite-plating process, material properties including CTE, Young's modulus, and hardness can be modified easily in the expected way. This work has provided an alternative material selection for the development of MEMS devices with optimum properties using nanocomposites.

Table 2.1 Plating bath conditions of Ni-based nanocomposites.

Ni-diamond nanocomposite	
DC plating bath:	
Nickel sulfamate (g/L)	400
Nickel chloride (g/L)	5
Boric acid (g/L)	40
Wetting agent (c.c.)	5
Concentration of diamond nanoparticles (g/L)	0.5, 1, 2
Average diameter of diamond nanoparticles (nm)	50, 125, 350
pH	4.1 ~ 4.3
Current density (mA/cm^2)	10
Temperature (°C)	50
Ni-SiO_2 nanocomposite	
DC plating bath:	
Nickel sulfamate (g/L)	400
Nickel chloride (g/L)	5
Boric acid (g/L)	40
Wetting agent (c.c.)	5
Concentration of SiO_2 nanoparticles (g/L)	0.008, 0.018, 0.036
Average diameter of SiO_2 nanoparticles (nm)	80
pH	4.1 ~ 4.3
Current density (mA/cm^2)	10
Temperature (°C)	50

Table 2.2 Parameters derived from XRD investigation on Ni-based nanocomposite.

	2θ (°)	**β (°)**	**D (nm)**	**d (Å)**	**ε_{macro} (%)**
* **Ni-diamond nanocomposite**	44.569	0.440	20.0	2.0313	-0.15
Pure electroplated Ni	44.498	0.431	20.5	2.0344	---
† **Ni-SiO_2 nanocomposite**	44.455	0.409	21.6	2.0362	0.09

* The average diameter and contraction of adding nano-diamond particles in plating bath are 350 nm and 2 g/L.

* The volume fraction of diamond in nanocomposite is 0.47%.

† The average diameter and contraction of adding SiO_2 nanoparticles in plating bath are 80 nm and 0.036 g/L.

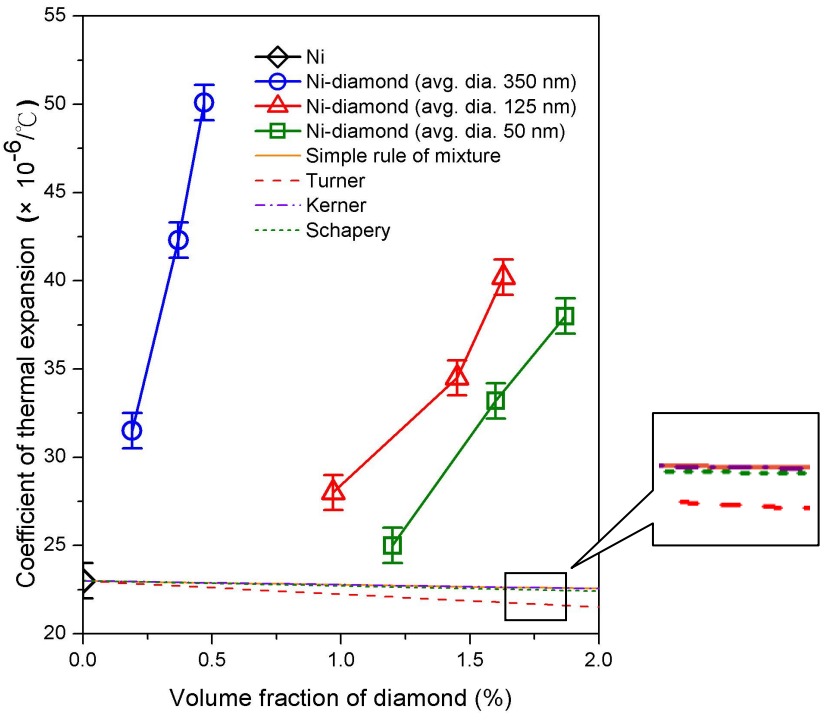

Figure 2.1 Comparison between experimentally measured data and theoretically predicted calculations of CTE values of Ni-diamond nanocomposites.

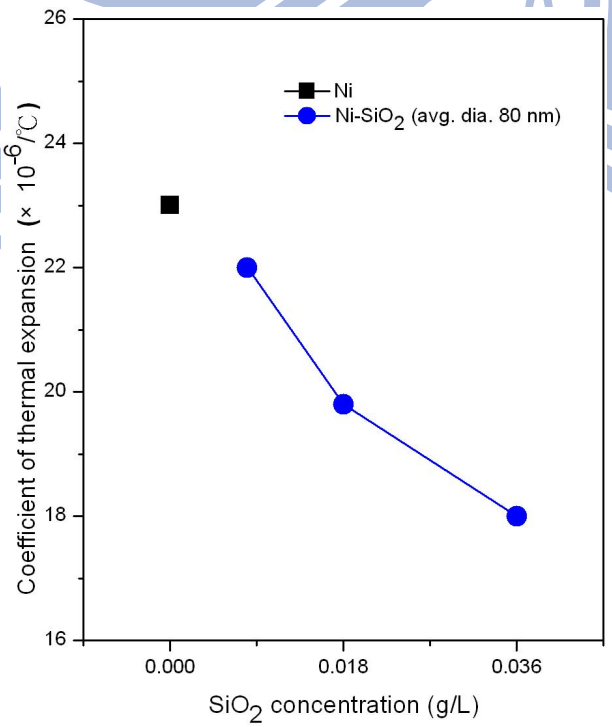

Figure 2.2 Comparison of CTE properties between pure electroplated Ni and Ni-SiO_2 nanocomposites with different particle concentration. [13]

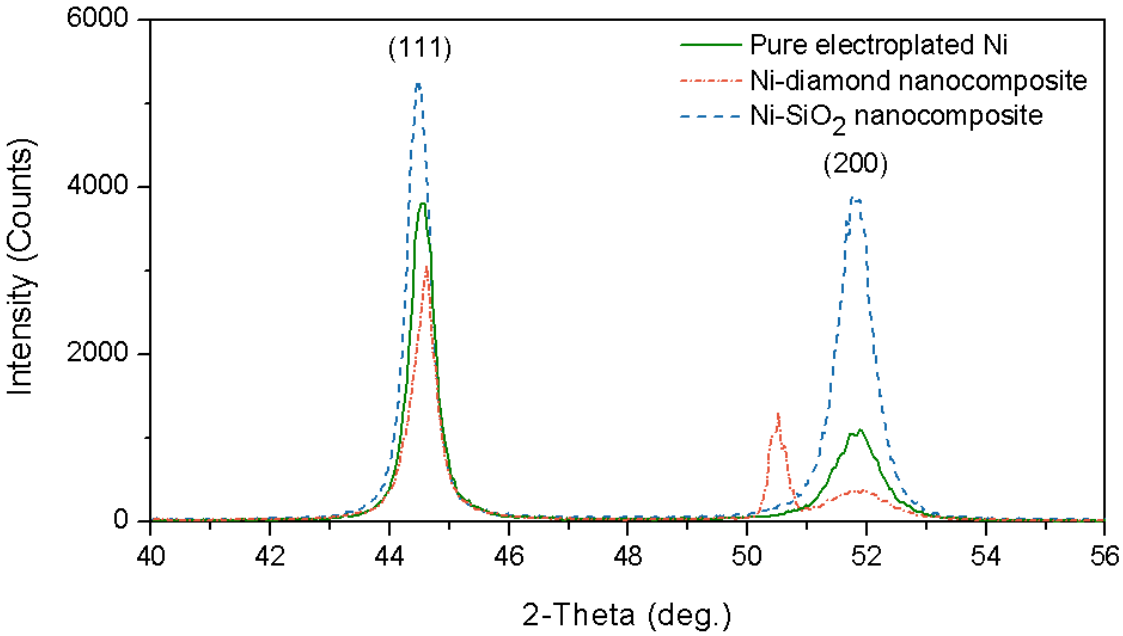

Figure 2.3 The XRD patterns at room temperature for the as-fabricated pure Ni, Ni-diamond (average particle size: 350 nm; particle concentration: 2 g/L), and Ni-SiO_2 (average particle size: 80 nm; particle concentration: 0.036 g/L) nanocomposites.

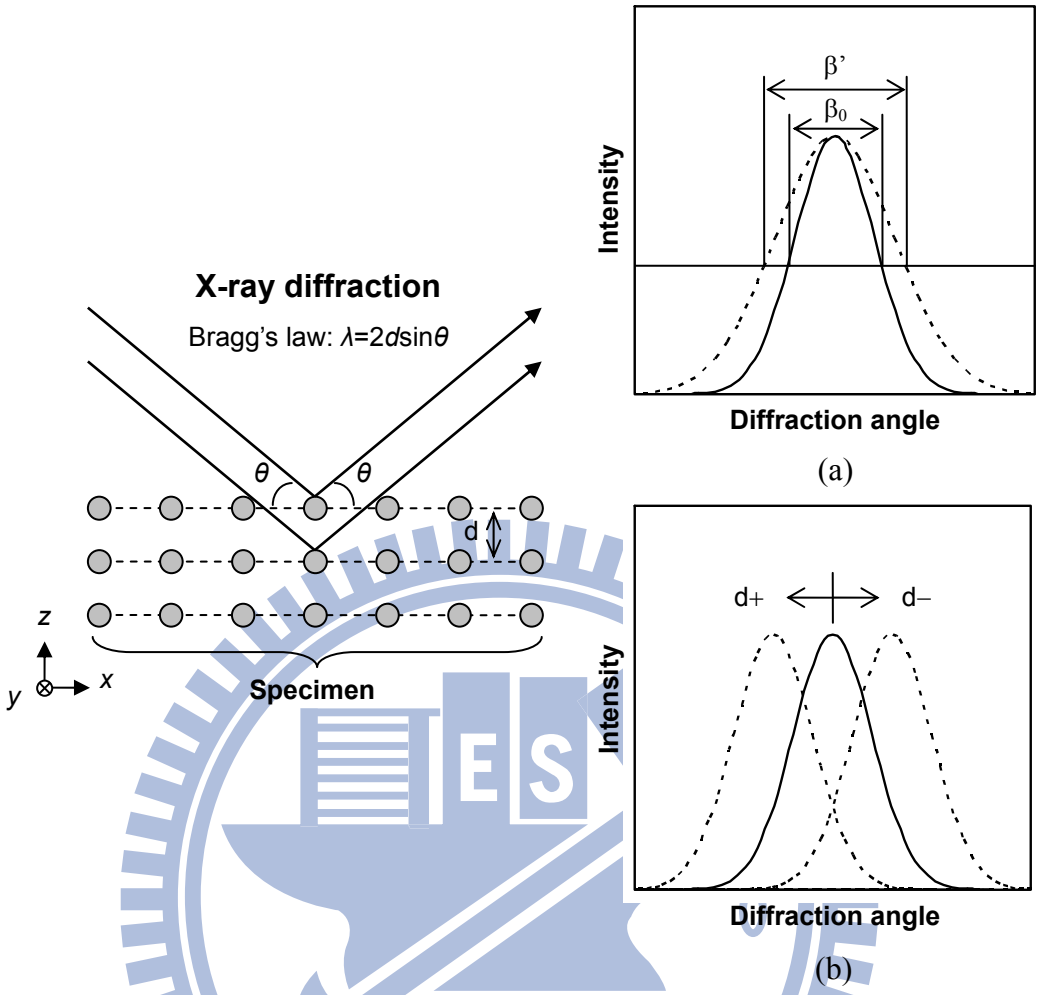

Figure 2.4 Principle of (a) microstrain measurement by XRD peak broadening; (b) macrostrain measurement by XRD peak shift.

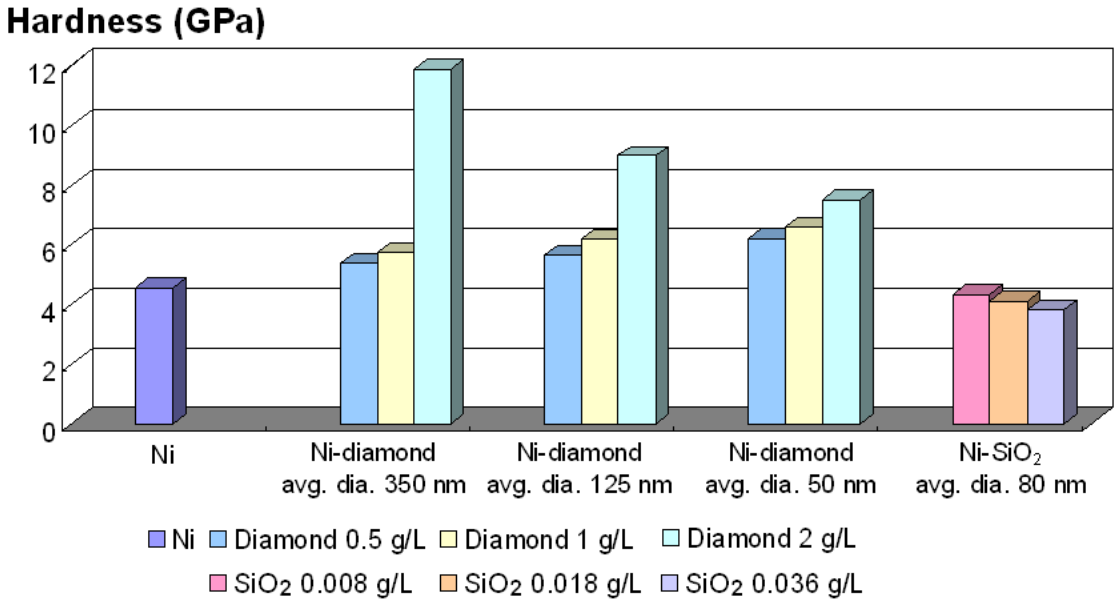

Figure 2.5 Comparison of hardness between electroplated Ni and Ni-based nanocomposites including Ni-diamond and Ni-SiO_2 with different particle sizes and concentrations. [12, 13]

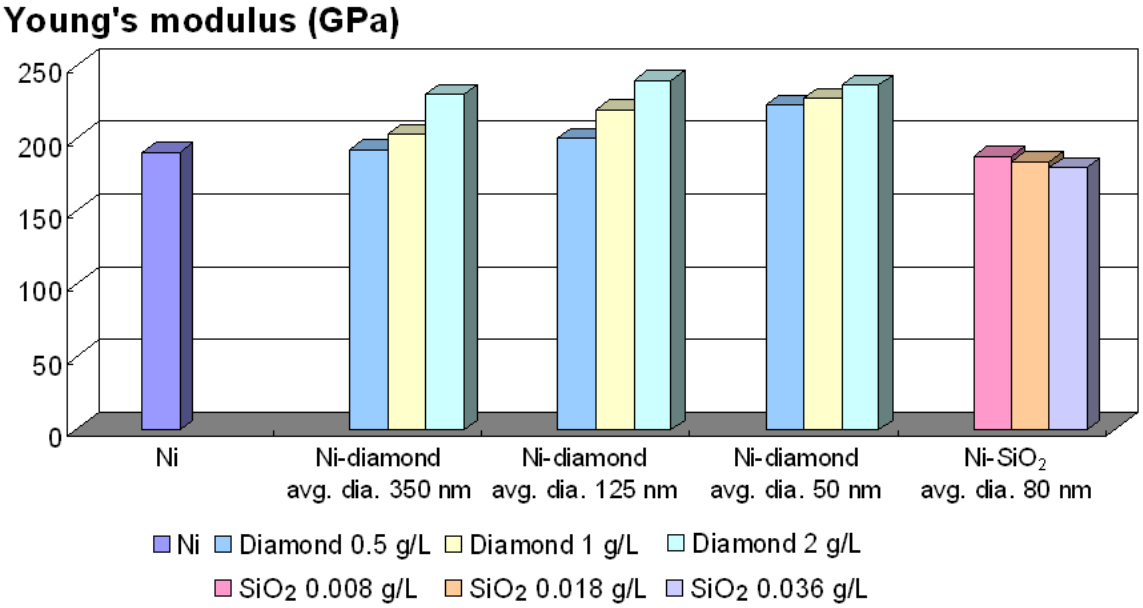

Figure 2.6 Comparison of Young's moduli between electroplated Ni and Ni-based nanocomposites including Ni-diamond and Ni-SiO_2 with different particle sizes and concentrations. [12, 13]

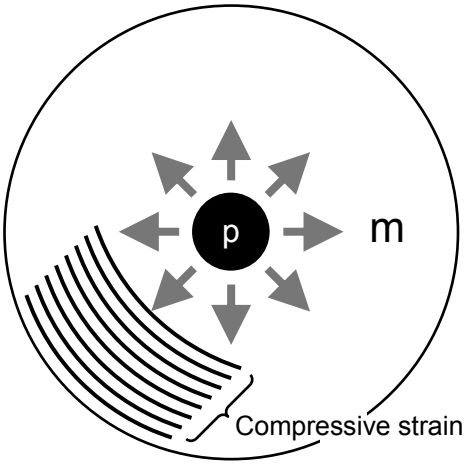

(a)

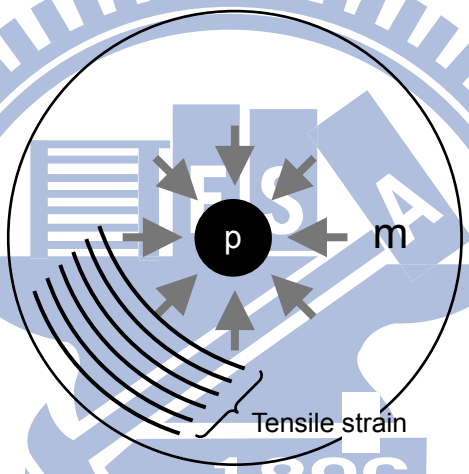

(b)

Figure 2.7 Resulted residual stress type from particle and matrix in Ni-based nanocomposite: (a) compressive stress in Ni-diamond; (b) tensile stress in Ni-SiO_2.

Chapter 3 Application of CTE Property on Bimorph Effect

3.1 Introduction

Bimaterial structure can provide thermally-bended deformation due to the CTE mismatch between two bonded materials, so-called bimorph effect [45, 46]. Upon this effect, the bimaterial structure based transducers can detect external stimulus of temperature change and provide temperature-driven output force simultaneously. To date, thermal bimaterial structure has been widely utilized in several MEMS devices, such as thermal sensor [47], stress sensor [48], biological sensor [49], microvalve [50], pumping membrane [51], tilting micromirror [52], microrelay [53], microswitch [54], etc. Nevertheless, thermal bimaterial structure typically will exhibit initial deformation once the structure is released. This deformation is resulted by the residual thermal stress [55-57] induced in structural fabrication where structural materials have different CTE and process temperatures. Delaminating is also a common issue that may happen on the interlamination through large residual stress and low cohesive energy [58-60] to reduce the lifetime and reliability of thermal bimaterial structure. For a bimaterial structure, by arranging the low-CTE layer on top, thermal upward actuation can be achieved [61, 62]. However, since metal usually has higher CTE comparing to nonmetal material, thermal upward actuation is difficult to achieve when the metal layer is deposited above the nonmetal layer [52-54, 57]. Thus, further investigations in terms of material and process selection and structure design are still required for future applications of thermal bimaterial structure.

In recent researches, Teh et al. found that the incorporation of nano-diamonds in electrolytic Ni matrix to form Ni-diamond nanocomposite could reduce the film residual stress and render the film more compressively [20]. Besides, the nanocomposite could

exhibit a higher CTE than that of electroplated Ni [12, 13]. Therefore, this study will investigate the bimorph effect of Ni/Ni-diamond nanocomposite bimaterial and propose a newly thermal bimaterial microactuator by employing the advantages of Ni-diamond nanocomposite. It is our belief that the proposed thermal device using the Ni/Ni-diamond nanocomposite bimaterial would have better interfacial bonding strength and smaller residual thermal stress since Ni and Ni-diamond nanocomposite have different CTE but similar crystal structure and process temperature. By controlling the plating sequence of Ni and Ni-diamond nanocomposite, the fabricated thermal bimaterial structure desired to have upward or downward bended deformation can also be easily achieved.

3.2 Bimaterial Structure Design

Figure 3.1 shows the scheme of thermal bimaterial structures made of Ni/Ni-diamond nanocomposite bimaterial including upward and downward deflection types for bimorph effect investigation. Upon the plating sequence of Ni and Ni-diamond nanocomposite, two deflection types of thermal bimaterial structures, including upward and downward types, are available. The designed length L of fabricated thermal bimaterial structure ranged from 200 μm to 1500 μm where the width w is fixed at 50 μm. The connecting beam is 50 μm long (L_c) and 30 μm wide (w_c). The thickness of Ni and Ni-diamond nanocomposite layers are determined according to the optimum thermomechanical sensitivity S_T defined as tip deflection d for a temperature change ΔT.

$$S_T = \frac{d}{\Delta T} \tag{3.1}$$

where d and following F are the thermally generated tip deflection and the output force of a thermal bimaterial structure, respectively. The deflection and force can be expressed by the following equations [45]:

$$d = \frac{3w_1w_2E_1E_2t_1t_2(t_1+t_2)(\alpha_1-\alpha_2)\Delta TL^2}{(w_1E_1t_1^2)^2+(w_2E_2t_2^2)^2+2w_1w_2E_1E_2t_1t_2(2t_1^2+3t_1t_2+2t_2^2)} \quad (3.2)$$

and

$$F = \frac{3\overline{EI}d}{L^3} = Kd \quad (3.3)$$

where E_i, α_i, w_i, and t_i (i=1, 2) are, respectively, Young's modulus, CTE, width, and thickness of each layer; L, $\overline{EI}$, and K are, respectively, the length, flexural rigidity and spring constant of thermal bimaterial structure, and ΔT is the temperature change.

A folded structure design is introduced into the thermal bimaterial structure to increase output force and to decrease the thermal vibrational noise. For thermal bimaterial structure, the amount of tip deflection is proportional to the square of the structure length as shown in Equation 3.2, so the thermal bimaterial structure becomes more sensitive with increased length of bimaterial structure as shown in Equation 3.1. However, lower spring constant resulting from an increased length also decreases the output force as shown in Equation 3.3 and increases the thermal vibrational noise as follows [47]:

$$d_n = \sqrt{2k_BTB/K\pi fQ} \quad (3.4)$$

where k_B is the Boltzmann constant, T is the absolute temperature, B is the measurement bandwidth, K is the cantilever spring constant, f is the resonance frequency, and Q is the quality factor of the resonance. Since a folded structure behaves like the structure of two beams connected in parallel which can have a higher spring constant due to larger width, a promising way to increase output force and sensitivity of the thermal bimaterial structure without a significant increase of the thermal vibrational noise is to connect multiple bimaterial cantilever beams in a folded manner.

Before the layer thickness determination of thermal bimaterial structure, cantilevers made of single layer of Ni and Ni-diamond nanocomposite are first fabricated to

characterize the CTE of material and to measure CTE mismatch. By measuring the elongation of cantilever in a heated chamber with temperature control, CTE of Ni and Ni-diamond nanocomposite are found to be 15.6 $\times 10^{-6}$/°C and 19.4 $\times 10^{-6}$/°C, respectively, where the diamond content of the corresponding nanocomposite film is 0.32% in weight fraction according to the EA measurement. The Young's modulus of the electroplated film is characterized by the nanoindenter (MTS Nano Indentor XP) [63]. The indentation depth is set as 1/10 film thickness, and the measured value is the average over twenty test points. The measured Young's moduli of Ni and Ni-diamond nanocomposite by means of a nanoindentation test are found to be 211.0 GPa and 224.1 GPa, respectively.

Based on Equation 3.1, Equation 3.2 and aforementioned material properties, for the upward type thermal bimaterial structure with L=1500 μm and w=50 μm, the calculated thermomechanical sensitivity as function of Ni layer thickness is shown in Figure 3.2, respectively. Then, the optimal Ni thickness t_2 is found to be around half of the Ni-diamond nanocomposite thickness t_1 for the maximum themomechanical sensitivity [64]. For instance, for a bimaterial with the structure of 3 μm thick Ni and 6 μm thick Ni-diamond nanocomposite, the themomechanical sensitivity can be designed as high as 640.2 nm/K with the flexural rigidity of 6.61×10^{-10} N·m^2, and the output force of 150.5 μN as ΔT=200 °C. Similarly, for downward type thermal bimaterial structure, the layer thickness of Ni and Ni-diamond nanocomposite are also determined to be 3 μm and 6 μm respectively.

3.3 Bimaterial Structure Fabrication

Figure 3.3 depicts the fabrication process of the proposed thermal bimaterial structure. Initially, the 0.5 μm thick SiO_2 on a silicon wafer with patterned etching windows is first coated with 5 μm thick AZP-4620 photoresist (PR) and patterned as sacrificial layer

(Figure 3.3(a)) After hard baking, it is followed by sputtering seed layer of 1000 Å Cu onto 200 Å Ti as adhesion layer. 15 μm thick AZP-4620 PR is then spin coated and patterned to form the plating mold of thermal bimaterial structure, as shown in Figure 3.3(b). For upward type thermal bimaterial structure, the 6 μm thick composite-plating of Ni-diamond layer is deposited first to construct the bottom layer of thermal bimaterial structure. Subsequently, 3 μm thick electroplated Ni is deposited to construct the top layer (Figure 3.3(c)). Table 3.1 shows the plating bath condition, and the plating temperatures of both layers are kept at 50 °C. For the composite-plating of Ni-diamond nanocomposite which is different from electroplated Ni, the nano-diamond particles with 350 nm in average diameter are added into a sulfuric based Ni plating bath for the co-deposition, and the concentration of the nano-diamond particles in plating bath is 2 g/L. Finally, the fabricated thermal bimaterial structure is released after stripping the sacrificial layer by acetone solution (Figure 3.3(d)), and the silicon underneath is removed by KOH solution (Figure 3.3(e)). For downward type thermal bimaterial structure, the fabrication process is similar to the upward one except switching the plating sequence of Ni-diamond nanocomposite and Ni in Figure 3.3(c). By controlling the plating sequence of Ni and Ni-diamond nanocomposite, two deflection types of thermal bimaterial structures including upward and downward are easily fabricated.

Figures 3.4(a) and 3.4(b) show the scanning electron microscope (SEM) pictures of the upward and downward types of fabricated thermal bimaterial structures. It is found that no initial deformation is observed as proposed due to the same low process temperature of electroplated Ni and Ni-diamond nanocomposite for lower residual thermal stress in thermal bimaterial structure.

3.4 Measurements and Discussions

3.4.1 Thermal Performance Measurement

Figure 3.5 illustrates the set-up for the thermal performance measurement of the fabricated thermal bimaterial structure in terms of tip deflection in thermal chamber. First, a chip with thermal bimaterial structure is placed on a heating system in a chamber with temperature controller, and the focused tip image of thermal bimaterial structure is captured by a charge-coupled device (CCD) through optical microscope with positional z-adjustment. As the thermal bimaterial structure is heated up, the structural tip will deflect and result in a focus change, which requires z-adjustment to search for a new focus to have a clear tip image. Thus, the micrometer-scale tip deflection of thermal bimaterial structure is determined by measuring the focus variation (ΔZ) and the measurement accuracy of ΔZ is about 0.5 μm on positional z-adjustment. The measured out-of-plane tip deflections of fabricated thermal bimaterial structures including upward and downward types with length of 800 μm, 1000 μm, and 1500 μm are observed with temperature change from 0 °C to 200 °C. The relationship between tip deflection and elevated temperature is plotted in Figures 3.6(a) and 3.6(b). According to the measured results of thermal performance, as structure length L=1500 μm and temperature change ΔT=200 °C, the measured tip displacement of upward and downward types can reach around 82.5 μm and -22.5 μm, respectively. In this condition, the themomechanical sensitivity and output force are calculated, respectively, to be 412.5 nm/K and 97.0 μN for upward type thermal bimaterial structure; and -112.5 nm/K and -26.5 μN for downward type one.

From above calculated results of upward type thermal bimaterial structure, the thermomechanical sensitivity and output force are smaller than the theoretical calculation; and the thermal performance in tip deflection of downward type is not as large as upward type. It seems that the CTE difference between Ni and Ni-diamond nanocomposite in the

thermal bimaterial structure is not equal to the cantilevers' that made of single material layer. Assuming material properties of bottom structural layers of thermal bimaterial structure are the same as cantilever's that made of single Ni or Ni-diamond nanocomposite layer. Using Equation 3.2 and the measured data of Figures 3.6(a) and 3.6(b), the CTE of the top structural layer of thermal bimaterial structure have been modified to fit the experiment data. Therefore, as shown in Table 3.2, the CTE of top structural layer of Ni in upward type is modified to be 16.9 $\times 10^{-6}$/°C which is 8.3% deviation from single Ni cantilever. Similarly, the CTE of top structural layer of Ni-diamond nanocomposite in downward type is modified to be 16.2 $\times 10^{-6}$/°C which is 16.5% deviation from single Ni-diamond nanocomposite cantilever.

Seed layer effect may be the major cause resulting in the aforementioned CTE variation. While Ni-diamond nanocomposite is used as the top structural layer of thermal bimaterial structure in downward type, the plating seed layer of Ni-diamond nanocomposite is a 3 μm thick electroplated Ni. On the contrary, as Ni-diamond nanocomposite is used as the bottom structural layer in upward type, the plating seed layer is 1000 Å sputtering Cu which is similar to single material cantilever. According to atomic force microscope (AFM) surface images of 6 μm Ni-diamond nanocomposite on 3 μm electroplated Ni and 1000 Å sputtered Cu seed layers as shown in Figures 3.7(a) and 3.7(b), respectively, the Ni-diamond nanocomposite electroplated on the Ni layer has a higher surface roughness value (Ra) than that on the sputtering Cu layer. The rougher surface could be attributed to the difference of grain structure of Ni-diamond nanocomposite that may vary with the different seed layers and so does the material property of CTE. Further material characterization is required for verification.

3.4.2 Interlaminar Reliability Test

Figures 3.8(a) and 3.8(b) show the side wall SEM pictures of two bimaterial structure types including upward and downward, respectively. Due to similar crystal structures of Ni-base between plating Ni and Ni-diamond nanocomposite, the outside interlaminar boundary of fabricated thermal bimaterial structure is not evident. Figure 3.9 also shows the bright field TEM image of cross section of fabricated thermal bimaterial structure that the interface boundary displays strong bonding as similar Ni crystal structure. To further investigate the bonding strength, the following vibration test [65] is performed.

As shown in Figure 3.10, a chip with the thermal bimaterial structure is placed and fixed on piezoelectric shaker which is controlled by waveform generator connected to MEMS motion analyzer (MMA G2^{TM}, Etec). The thermal bimaterial structure is driven by an external piezoelectric shaker at destructive resonant frequency of the 5th vibration mode (the first torsion shape) obtained from the modal analysis by the commercial finite-element-analysis (FEA) software ANSYS. For the upward type with 1000 μm length, the 5th resonant frequency is about 108.2 kHz with 0.90 ±0.05 μm amplitude monitored by an interferometer connected to MMA, as shown in Figure 3.11. Because the delaminated interface has higher influence on the decrement of the resonant frequency of higher order modes, the shift in resonant frequency of the 5th vibration mode is detected to investigate the delamination between interlaminar layers of thermal bimaterial structure. The vibration test result is plotted in Figure 3.12 that the resonant frequency is found to be unchanged during 10^9 cycles of continuous vibration. In general, the infinite life of material is defined as no failure happened after $10^6 \sim 10^7$ cycles in fatigue test [66]. In this study, the test is only performed up to 10^9 cycles, and the measured resonant frequency remains unchanged after 10^9 cycles. This result shows good interlaminar bonding ability

between electroplated Ni and Ni-diamond nanocomposite since two materials in the thermal bimaterial structure are Ni-based.

3.4.3 Electro-thermal Driven Discussion

If the aforementioned bimaterial structures will be used for microactuation application, several design issues should be addressed. In general, electro-thermal microactuators are driven by electric heating, the driving energy Q and the generating temperature change ΔT can be expressed as follows:

$$Q = \frac{V^2 \Delta t}{R} = mC\Delta T \tag{3.5}$$

and

$$\Delta T = \frac{V^2 \Delta t}{R \cdot mC} = \frac{V^2 \Delta t}{\rho \frac{L'}{A} \cdot (L' AD \cdot C)} = \frac{V^2 \Delta t}{\rho DCL'^2} \tag{3.6}$$

where V, R, Δt, m, L', and A are, respectively, driving voltage, electrical resistance, heating time, mass, total length and cross-sectional area of electro-thermal microactuator. ρ, D, and C are electrical resistivity, density, and specific heat of structural material, respectively. Therefore, while supply voltage is applied to the bimaterial structure, the layer with lower electrical resistivity, i.e. pure Ni layer (1.59×10^{-5} Ω-cm, as measured by four-point probe), will have larger temperature change than that of Ni-diamond nanocomposite (1.87×10^{-5} Ω-cm, as measured). Since the CTE of Ni is smaller than that of Ni-diamond nanocomposite, the different temperature change to each structural layer will affect the thermal performance in terms of tip deflection due to the neutralization of the thermal elongations of Ni and Ni-diamond nanocomposite. Similarly, this problem also happens to the bimaterial structure of metal/p^+-Si and metal/poly-Si while it is utilized as an electro-thermal microactuator [46, 54, 57, 67]. In order to prevent the occurrence of neutralization, an insulated layer, such as oxide and nitride, is

generally used to assure only one heating layer. However, the insulated layer may cause the delamination in the thermal bimaterial structure to reduce the lifetime and reliability of microactuator as mentioned before.

Although the neutralization is unavoidable in the Ni/Ni-diamond nanocomposite bimaterial structure without having an insulated layer in between, it could be solved further by controlling the diamond concentration in the Ni-diamond nanocomposite to keep both layers have the same temperature change, i.e. $\Delta T_{Ni-d} = \Delta T_{Ni}$ during electric heating. From Equation 3.6, as $\Delta T_{Ni-d} = \Delta T_{Ni}$, it can be found that $\rho_{Ni-d} D_{Ni-d} C_{Ni-d} = \rho_{Ni} D_{Ni} C_{Ni}$. According to the rule of mixtures [21], the incorporation of diamond will result in the increase of Ni electrical resistivity and the decrease of Ni density simultaneously. By well controlling the total amount of incorporated nano-diamonds, the multiple of electrical resistivity, density, and heat capacity can be the same to both materials. Thus, the correlation between material properties and nano-diamond concentration requires further investigation for optimal microactuation using the Ni/Ni-diamond bimaterial structure.

3.5 Summary

Thermal bimaterial structures made of electroplated Ni and Ni-diamond nanocomposite for CTE mismatch are fabricated successfully to achieve upward and downward out-of-plane displacement easily by controlling the plating sequence of electroplated Ni and Ni-diamond nanocomposite. Due to the same low process temperature (~50 °C) of electroplated Ni and Ni-diamond nanocomposite, the residual thermal stress and initial deformation of fabricated thermal bimaterial structures are small. Since two materials in the thermal bimaterial structure are Ni-based, the fabricated thermal bimaterial structure also shows good interlaminar bonding ability between electroplated Ni and Ni-diamond nanocomposite. In addition, electroplated Ni and Ni-diamond

nanocomposite are compatibility with MEMS and CMOS fabrication technologies via a one-step and selective on-chip deposition process at low temperatures (~50-90 °C). Therefore, thermal bimaterial structure made of electroplated Ni and Ni-diamond nanocomposite can be integrated into MEMS and CMOS fabrication process for sensor and actuator application.

Table 3.1 Plating bath conditions of Ni and Ni-diamond nanocomposite for structural layers of thermal bimaterial structure.

Electroplating: Ni	
DC plating bath:	
Nickel sulfamate (g/L)	400
Nickel chloride (g/L)	5
Boric acid (g/L)	40
Wetting agent (c.c.)	5
pH	4.1 ~ 4.3
Current density (mA/cm^2)	10
Temperature (°C)	50
Composite-plating: Ni-diamond nanocomposite	
DC plating bath:	
Nickel sulfamate (g/L)	400
Nickel chloride (g/L)	5
Boric acid (g/L)	40
Wetting agent (c.c.)	5
Concentration of diamond nanoparticles (g/L)	2
Average diameter of diamond nanoparticles (nm)	350
pH	4.1 ~ 4.3
Current density (mA/cm^2)	10
Temperature (°C)	50

Table 3.2 CTE and Young's modulus of each structural layer of thermal bimaterial structures.

Type	**CTE (×10^{-6}/°C)**		**Young's modulus (GPa)**	
	Bottom layer	Top layer	Bottom layer	Top layer
Upward	19.4	16.9	224.1	219.7
	Ni-diamond	Ni	Ni-diamond	Ni
Downward	15.6	16.2	211.0	234.9
	Ni	Ni-diamond	Ni	Ni-diamond

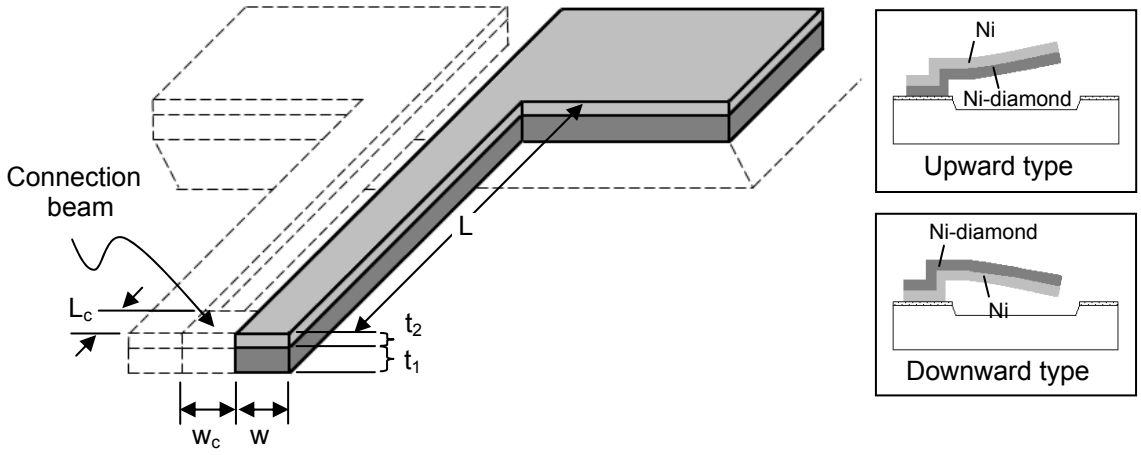

Figure 3.1 Schematic illustration of Ni-based thermal bimaterial structures including upward and downward deflection types.

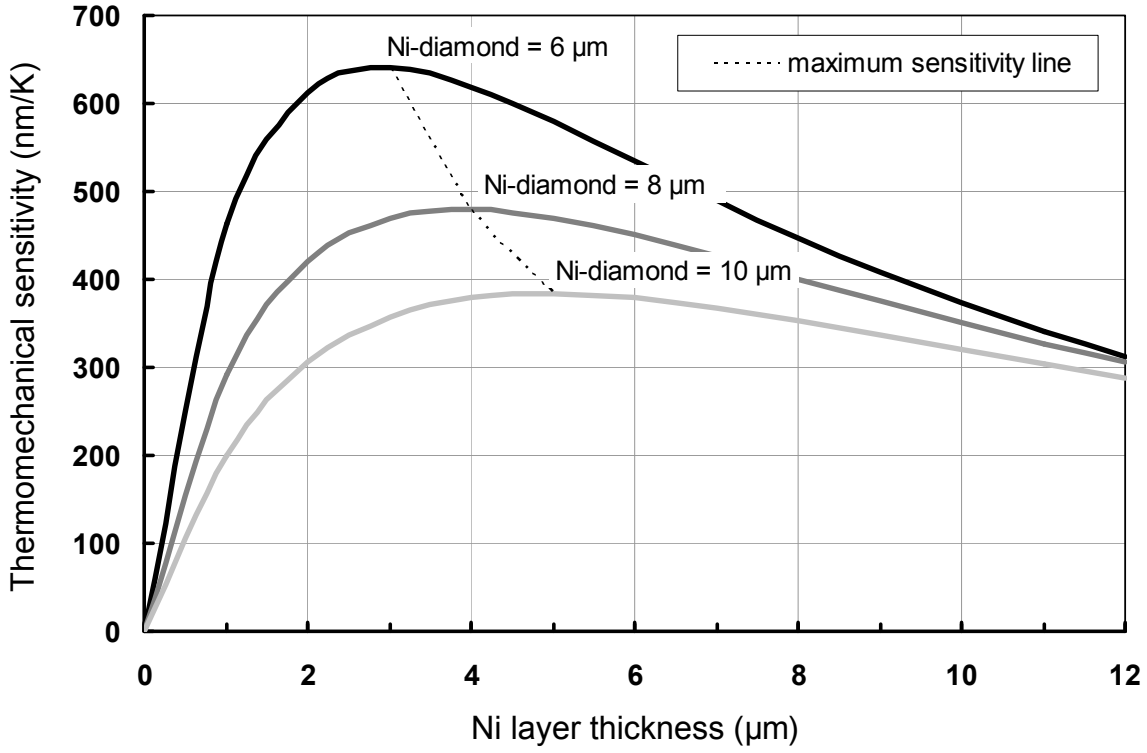

Figure 3.2 Calculated themomechanical sensitivity of thermal bimaterial structure for layer thickness determination.

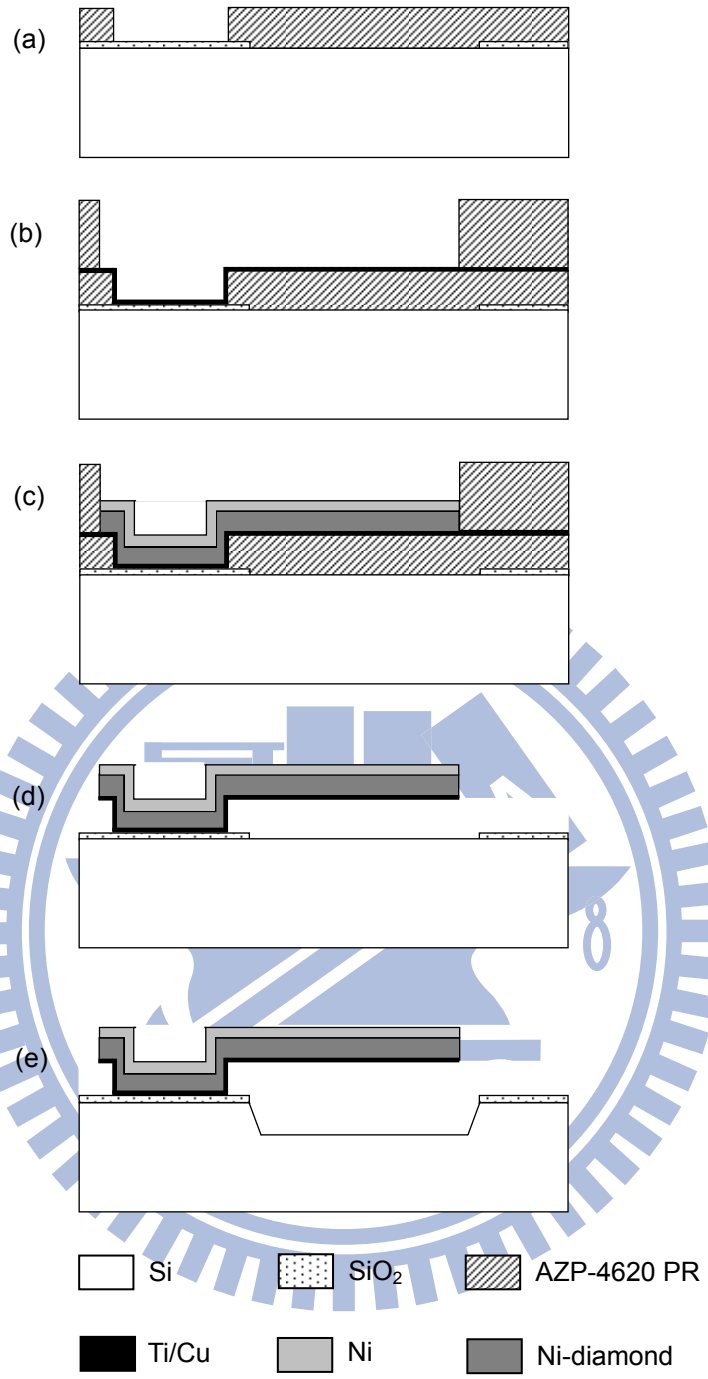

Figure 3.3 Fabrication process of thermal bimaterial structure: (a) 5 μm AZP-4620 PR deposition and patterning; (b) sputtered Ti/Cu as an adhesion and seed layer, then 15 μm AZP-4620 PR deposition and patterning as the plating mold structure; (c) layers electroplating: Ni-diamond nanocomposite for bottom layer, and Ni for top layer (i.e. upward type); (d) structure releasing; (e) silicon removing by KOH.

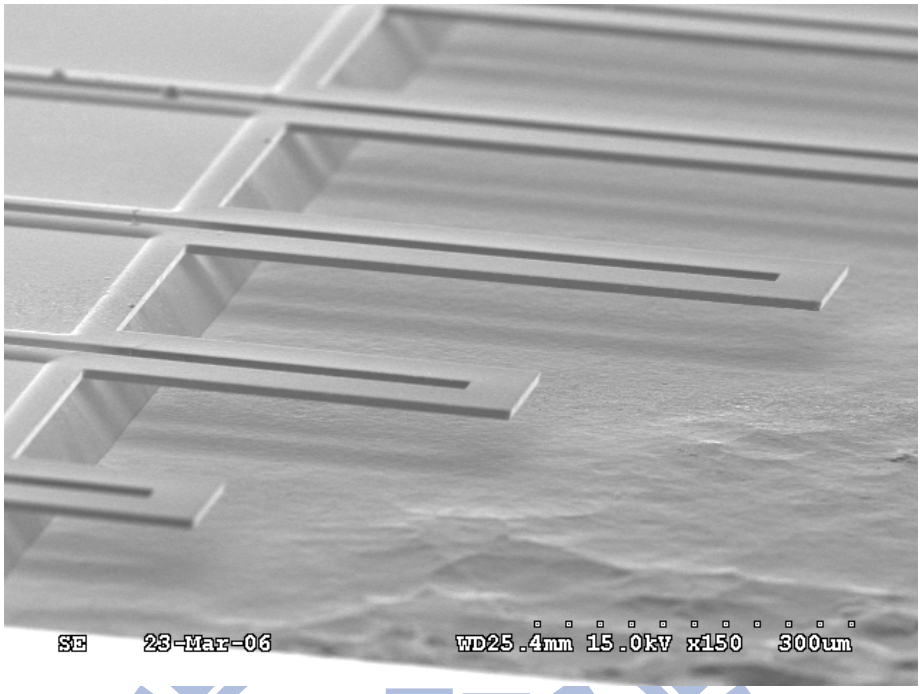

(a)

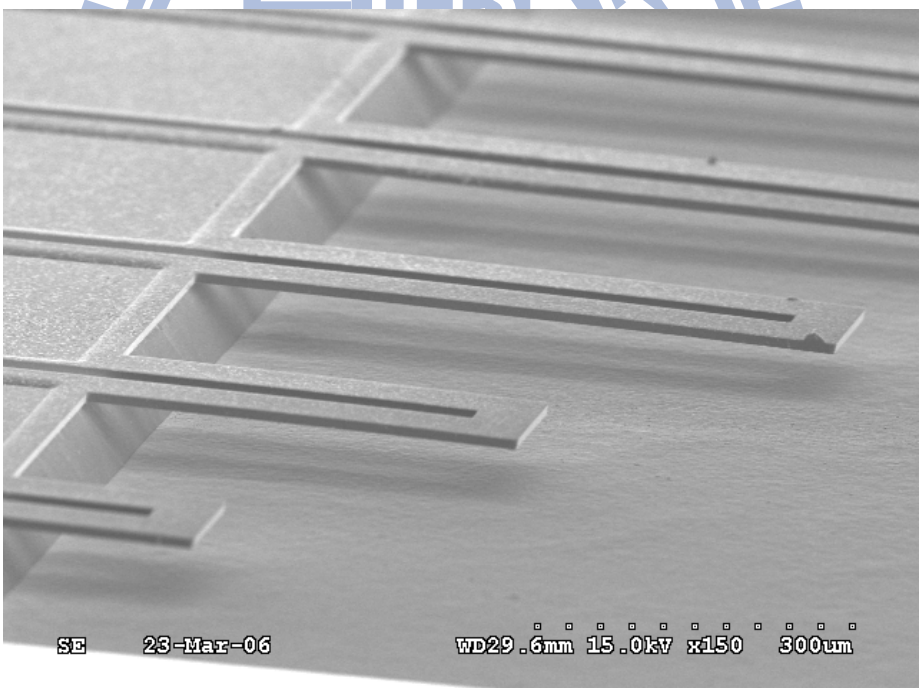

(b)

Figure 3.4 SEM pictures of fabricated thermal bimaterial structures: (a) upward type: Ni layer on top of Ni-diamond nanocomposite layer; (b) downward type: Ni-diamond nanocomposite layer on top of Ni layer.

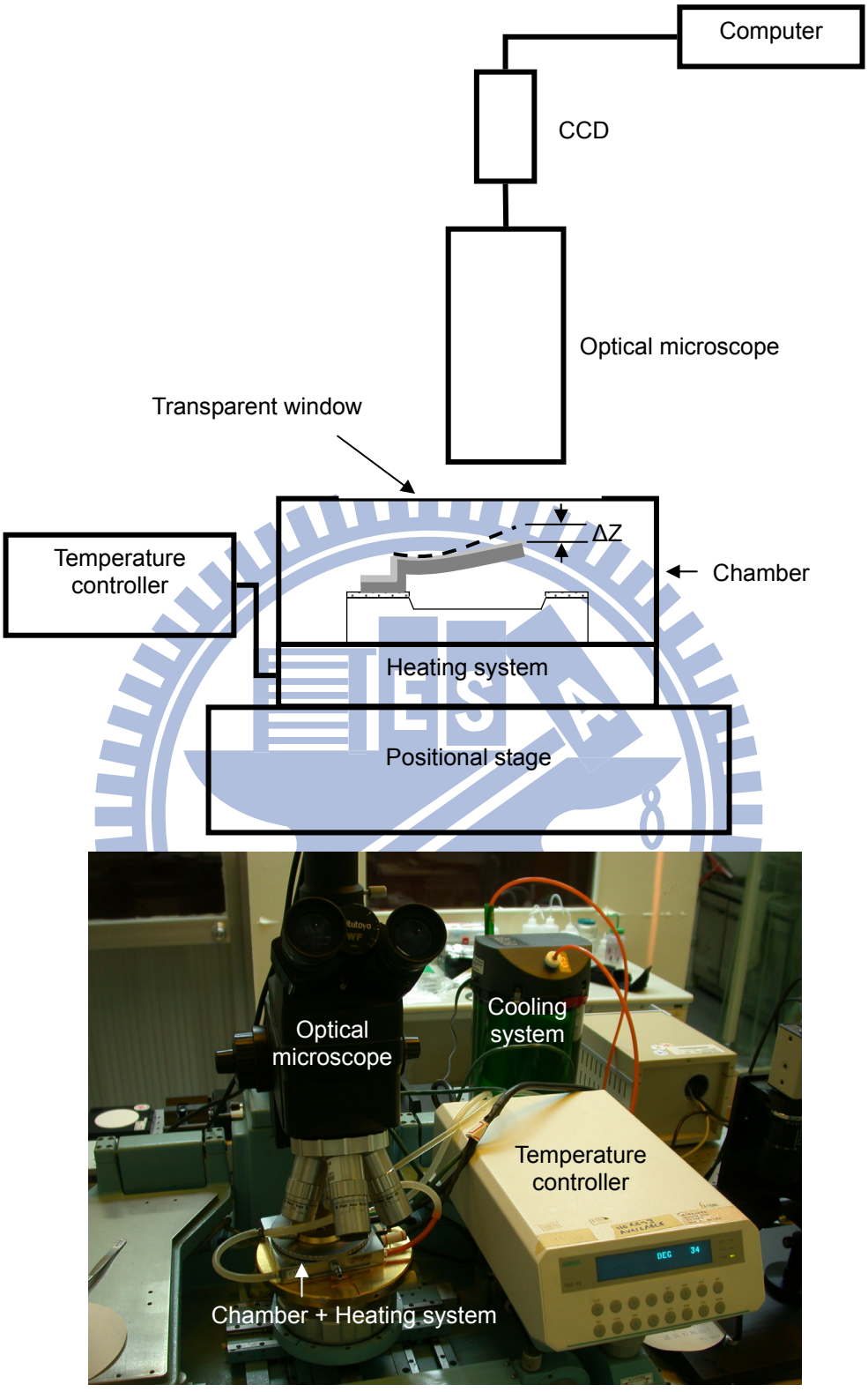

Figure 3.5 Schematic diagram and photo of set-up for thermal performance measurement of thermal bimaterial structure.

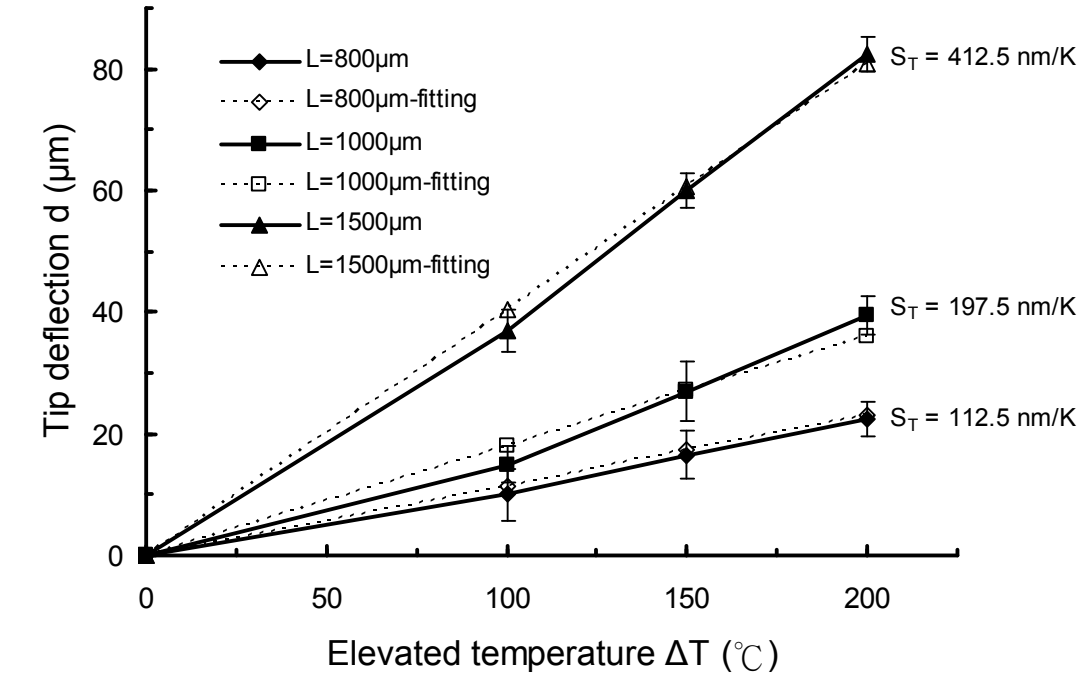

(a)

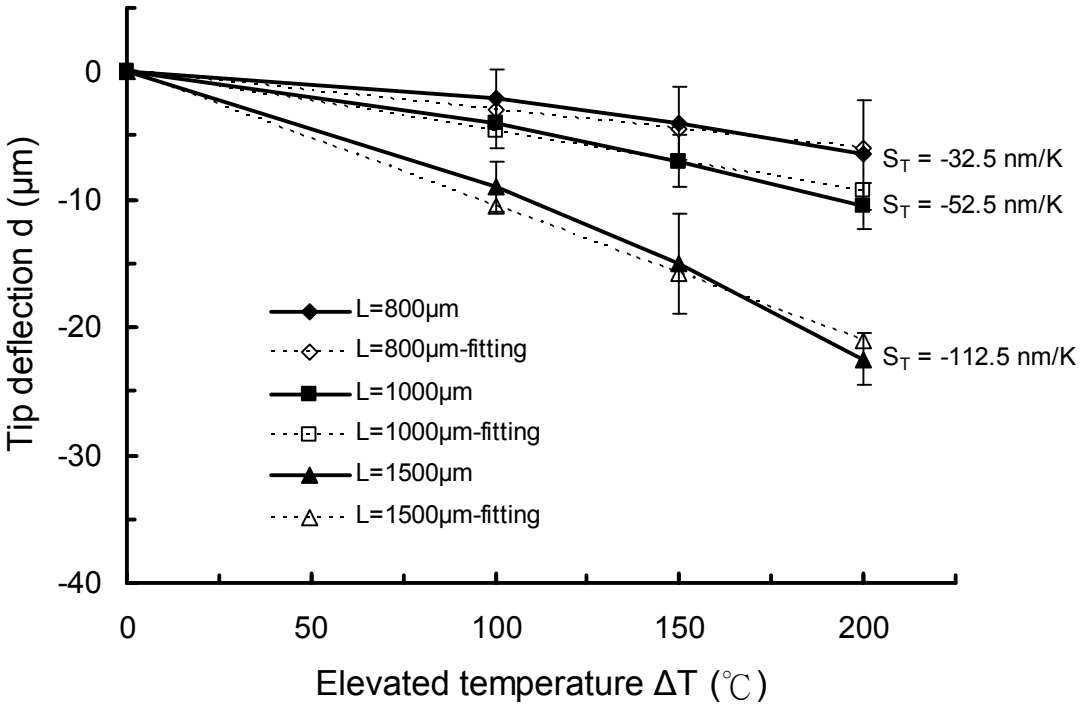

(b)

Figure 3.6 Thermal performance measurement results and fitting curves in terms of the tip deflection of thermal bimaterial structure at elevated temperature: (a) upward type; (b) downward type.

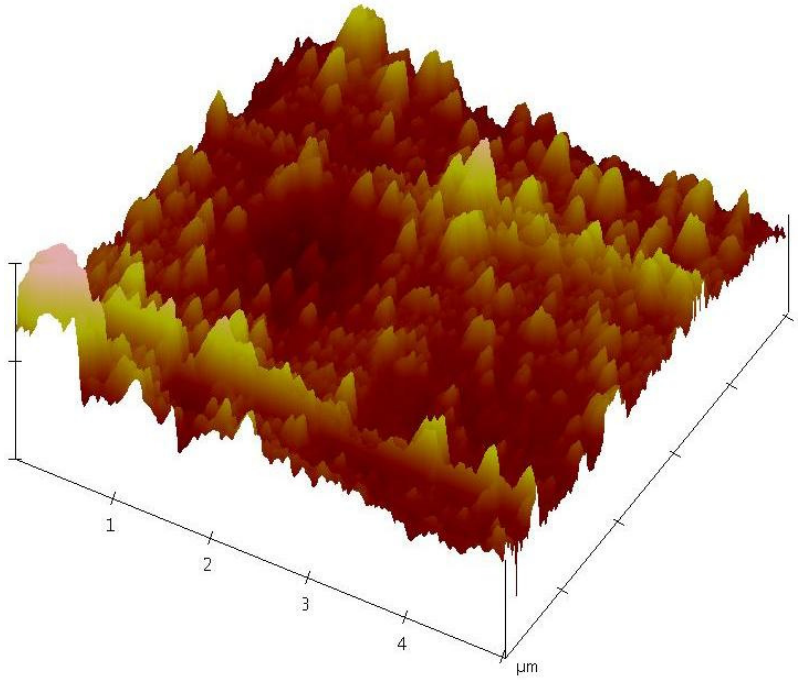

(a)

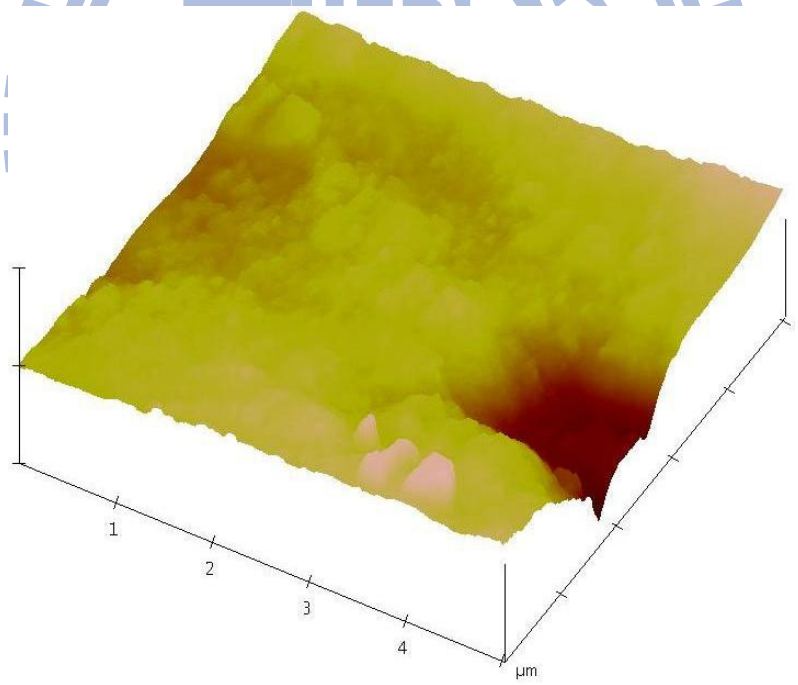

(b)

Figure 3.7 AFM surface images of 6 μm Ni-diamond nanocomposite layer on the top of (a) 3 μm electroplated Ni layer, Ra=15.313 nm; (b) 1000 Å sputtering Cu layer, Ra=5.275 nm. X: 1 μm/div; Z: 200 nm/div.

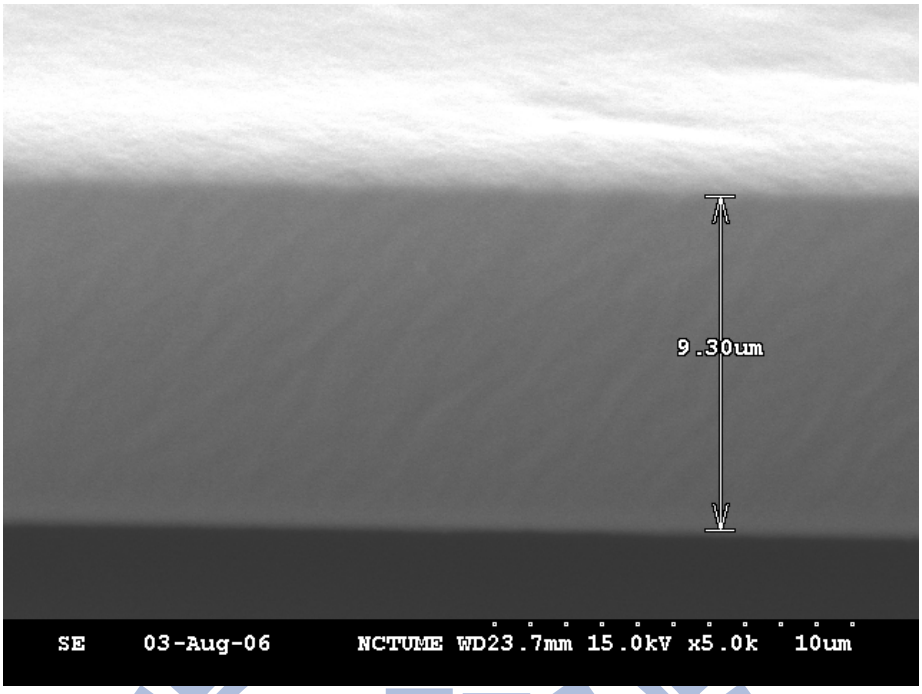

(a)

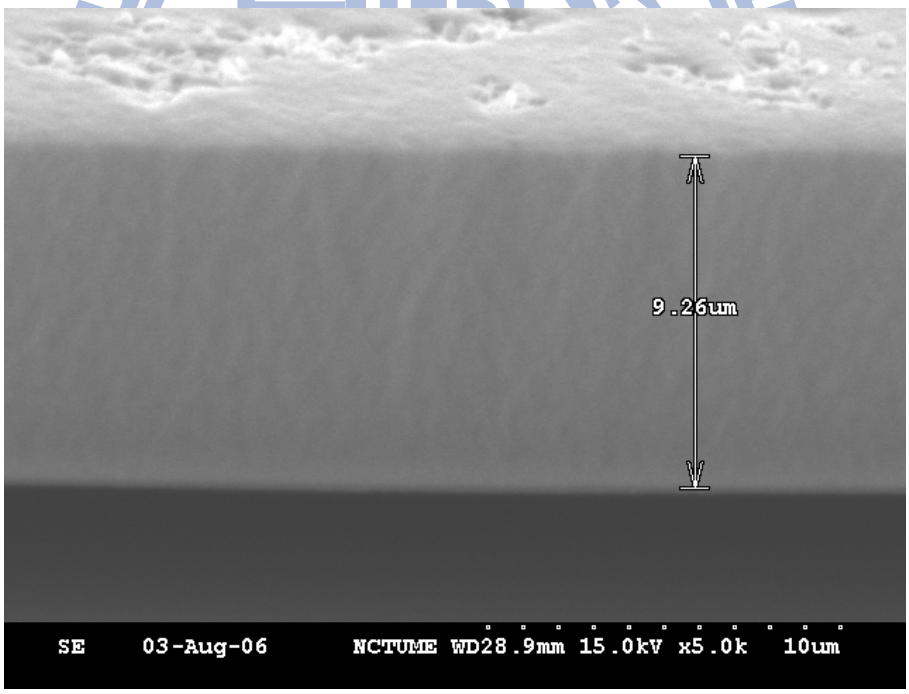

(b)

Figure 3.8 Side wall SEM pictures of fabricated thermal bimaterial structures: (a) upward type; (b) downward type.

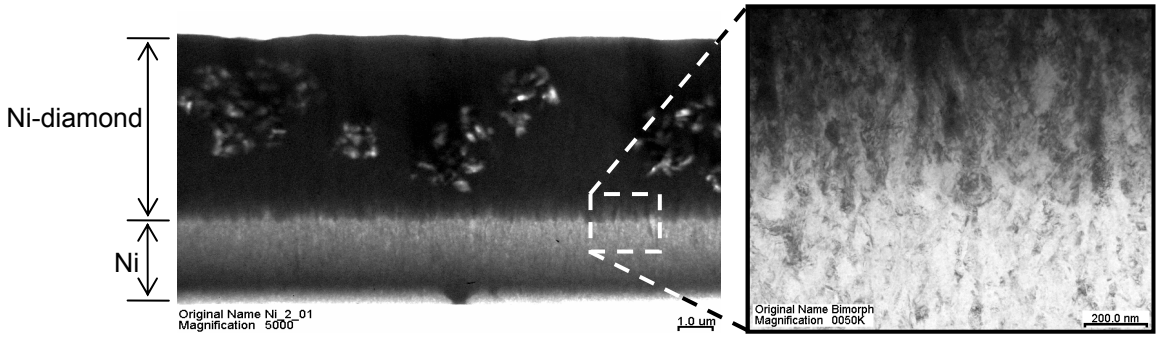

Figure 3.9 TEM images of cross section of fabricated thermal bimaterial structure and interface boundary between layers of Ni and Ni-diamond nanocomposite.

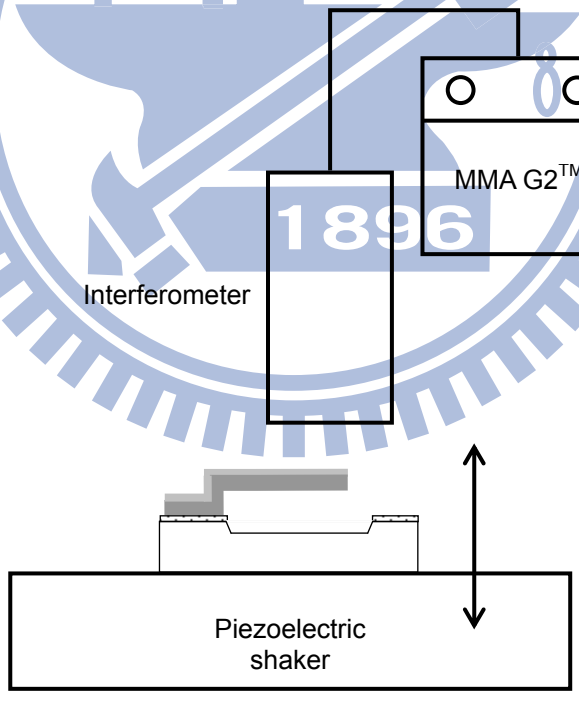

Figure 3.10 Schematic diagram of set-up for interlaminar reliability test.

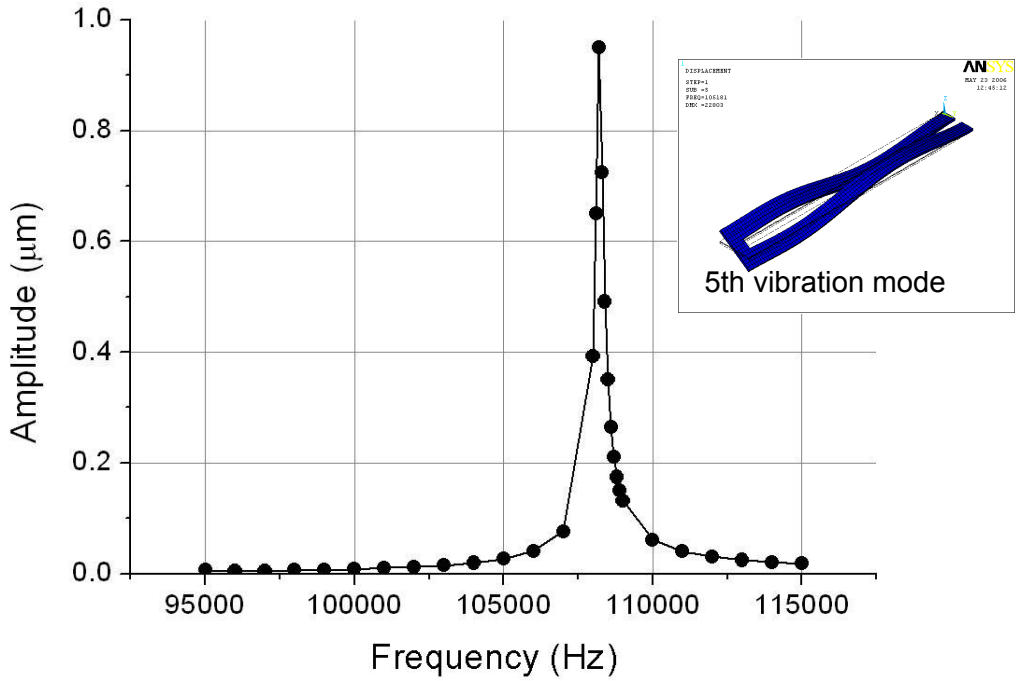

Figure 3.11 The 5th resonant frequency of thermal bimaterial structure with 1000 μm long upward type measured by MMA.

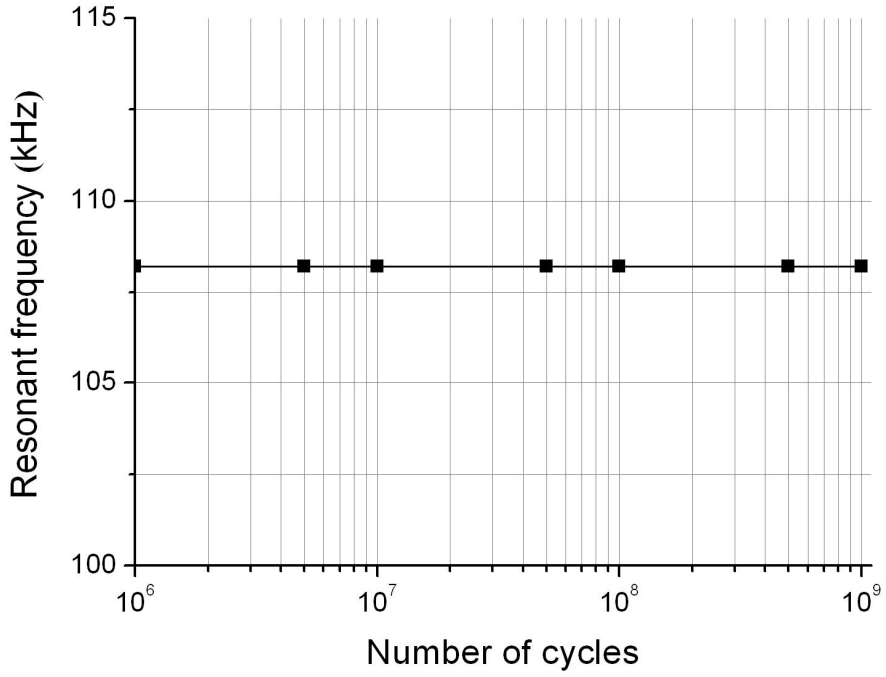

Figure 3.12 Resonant frequency detection of thermal bimaterial structure in 10^9 vibration cycles.

Chapter 4 Investigation on Fatigue Property

4.1 Introduction

Nanotechnology has advanced the electro-deposition technique for high performance MEMS fabrication in terms of material property enhancement by nanocomposite effect [7]. In previous researches, the electrolytic Ni matrix with the incorporation of nano-diamonds could exhibit higher Young's modulus, hardness, and CTE [12-14]. Via the property modification based on the nanocomposite effect, MEMS devices made of the nanocomposite can have superior performance. For example, Tsai et al. [12, 13] found that electro-thermal microactuator made of Ni-diamond nanocomposite could have 73% power consumption saving in comparison with that made of pure Ni for the same output displacement via the CTE enlargement of structural material. In addition, more than 67% ultimate elongation could be achieved. Lee et al. [14] demonstrated that μ-resonator made of Ni-diamond nanocomposite could have higher resonance frequency than the pure Ni one due to Young's modulus improvement on structural material, which could be helpful in RF-MEMS application. Therefore, Ni-diamond nanocomposite has been shown to have potential as the structure material for MEMS devices. In the further design and application of MEMS devices, especially for moving components under cyclic load, it will be essential to investigate the fatigue behavior on the structural materials. However, up to now, the related fatigue behavior of the electroplated Ni-diamond nanocomposite has not been well studied and reported yet.

To date, a variety of testing methods have been proposed for the fatigue characterization of microsized materials. Among these methods, tensile and bending tests are two popular testing schemes. Tensile method [22, 23] can extract Young's modulus and fracture strength directly from the measured stress-stain curve. However, once the

sample becomes very small only with several millimeters, the setup requirements for gripping, aligning, and pulling a tested sample become stringent to the method [68]. In comparison with the tensile method, bending method [25, 69, 70] can be free of the issues raised by sample gripping and alignment. Furthermore, bending test only requires smaller loading force than that of tensile test to yield tested sample with enough deformation for accurate measurement, which makes the method suitable for thin film characterization.

Thus, in order to further study the reliability issue, a fatigue characterization scheme based on the bending-test design is proposed and utilized for the property investigations on the Ni-based nanocomposites, which are incorporated with different particle sizes (i.e. 350 nm and 50 nm in diameter), in terms of Young's modulus, fatigue lifetime, fatigue strength, and fracture mechanism.

4.2 Experiment Setup

Figure 4.1 shows the scheme of the bending-fatigue test where a microsized cantilever-beam specimen is tested in a displacement-control mode. A tungsten micro-probe is controlled by the test machine (μMTS Tytron 250) to cyclically exert a loading force on the free-end of cantilever beam with a fixed vertical displacement [70]. Before sample testing, the contact detection between micro-probe and microsized cantilever-beam specimen is conducted by the load cell underneath the tested specimen. Through the load cell fixed on a precise x-y table and the CCD system, the micro-probe can accurately be placed on the right load-position of microsized cantilever-beam specimen. In this fatigue test machine, the resolutions of load cell and displacement actuation can be controlled at 0.1 mN and 0.1 μm, respectively. Figure 4.2 shows the illustration of microsized cantilever-beam specimen for bending-fatigue test. A contact hole is introduced in the specimen design at the load-position to fix the micro-probe with

specimen for preventing the probe-tip from gliding along the beam during the test [71]. The contact hole (15 μm in diameter) is located on the center line of cantilever beam with 130 μm from the root of the beam and 50 μm from the free-end. The designed width (w) and thickness (t) of the microsized cantilever-beam specimen are fixed at 50 μm and 15 μm, respectively.

4.3 Specimen Preparation

Figure 4.3 depicts the fabrication process of the microsized cantilever-beam specimen on the silicon substrate. Initially, the Ti adhesion layer (200 Å thick) and Cu seed layer (1000 Å thick) are sputtered respectively onto the cleaned silicon wafer. Then, the 20 μm thick AZP-4620 photoresist (PR) is coated and patterned to form the plating mold of microsized cantilever-beam specimen (Figure 4.3(a)). Subsequently, the electroplated Ni-based material is deposited by DC plating to construct the microsized cantilever-beam specimen (Figure 4.3(b)). Table 4.1 shows the plating bath conditions of electroplated Ni-based materials of pure Ni and Ni-diamond nanocomposites. For the composite-plating of Ni-diamond nanocomposites which are different from pure electroplated Ni, the nano-diamond particles with the average particle-diameters of 350 nm and 50 nm are added respectively into the different plating baths of sulfuric-based Ni for the co-deposition. The concentration of nano-diamond particles in each composite-plating bath is kept at 2 g/L. Finally, the fabricated cantilever-beam specimen is released after stripping the plating mold by acetone solution (Figure 4.3(c)), which is followed by the removal of silicon underneath using the wet-etching process with KOH solution (Figure 4.3(d)).

Figure 4.4 shows the SEM pictures of as-fabricated cantilever-beam specimens made of electroplated Ni and Ni-diamond nanocomposites for the bending-fatigue test.

According to the EA measurements of Ni-diamond nanocomposites, the diamond content of the corresponding nanocomposite films with the average particle-diameters of 350 nm and 50 nm are 0.14% and 0.16% in weight fraction, respectively. Furthermore, according to the calculation based on the density of Ni (8908 kg/m^3 [12]) and diamond (3510 kg/m^3 [12]), the diamond content of Ni-diamond nanocomposite films with the average particle-diameters of 350 nm and 50 nm are 0.35% and 0.41% in volume fraction, respectively.

4.4 Measurements and Results

4.4.1 Static Bending Test

Before the fatigue test, a static bending test is performed on the as-fabricated cantilever nanocomposite beam to determine the displacement loading condition of fatigue test. A tungsten micro-probe tip connected to the test machine is precisely placed at the contact hole of the tested beam, and the loading force applied by the probe to the beam is measured by a load cell connected to the computer. The tested beam is then gradually deflected by the micro-probe tip from 0 μm to 50 μm with the increment of 2 μm, so the loading displacement versus corresponding force can be recorded by the computer as shown in Figure 4.5, so-called force-displacement ($F-\delta$) curve. In our observation, after the 50 μm deflection in static bending test, the permanent deformation had occurred on each tested beam but no obvious fractures could be found under SEM. Therefore, for the later fatigue test, the maximum displacement loading (δ_{max}) is estimated by the proportional limit of $F-\delta$ curve in Figure 4.5, which is about 18 μm in this study.

4.4.2 Young's Modulus Measurement

According to the Figure 4.5, the slope of $F-\delta$ curve also indicates that the incorporation of nano-diamonds in Ni matrix can enhance the stiffness (i.e. the ratio of force to displacement) of specimen over that of pure electroplated Ni. Using the stiffness data, the Young's modulus of specimen material can be extracted from the following cantilever-beam equation [72]:

$$E = \frac{L^3}{3I} \cdot \frac{F}{\delta} \tag{4.1}$$

where L is the length from the beam-root to the load-position, and I is the moment of inertia. However, the above equation is only derived from an idea case without considering actual boundary conditions like quarter-plane and undercut [73] which usually occurred in the wet-etching process with KOH solution, so that the extracted Young's modulus becomes unreasonable. In order to solve this problem, commercial FEA software, ANSYS, is employed to estimate the accurate Young's moduli of the tested samples. Through the model construction based on the actual parameters of tested beam size and undercut size, the analytical stiffness can be derived from ANSYS simulation. Comparing with the experimental stiffness calculated from Figure 4.5, once the analytical data is matched with the experimental one, the corresponding Young's modulus can be obtained. Thus, the corresponding Young's moduli of tested samples are found to be 156.9 GPa, 165.9 GPa, and 178.2 GPa of electroplated Ni and Ni-diamond nanocomposites with the average particle-diameter of 350 nm and 50 nm, respectively.

To further examine the correctness of the derived Young's moduli from $F-\delta$ curves, the following methods including nanoindenter measurement [63] and resonant frequency detection [74] are performed. Using the measurement equipment of nanoindenter (MTS Nano Indentor XP), the Young's modulus is characterized directly from the electroplated film. The indentation depth is set as 1/10 film thickness, and the

measured value is the average over twenty test-points. Thus, by means of indentation test, the measured Young's moduli of the electroplated Ni and Ni-diamond nanocomposites with the average particle-diameter of 350 nm and 50 nm are found to be 156.7±5 GPa, 164.0±5 GPa, and 178.0±5 GPa, respectively. Subsequently, using the measurement equipment of laser Doppler vibrometer (LDV, Ono Sokki LV-1710), the resonant frequency of the electroplated cantilever beam can be detected. Through the comparison between the detected resonant frequency from LDV and the analytical resonant frequency from foregoing FEA model, once the analytical data is matched with the detected one, the corresponding Young's modulus can be characterized. Thus, the corresponding Young's moduli of tested specimens are found to be 158.1±2 GPa, 163.3±2 GPa, and 178.2±2 GPa of the electroplated Ni and Ni-diamond nanocomposites with the average particle-diameter of 350 nm and 50 nm, respectively.

According to the above measurement results, the derived Young's moduli from nanoindenter measurement and resonant frequency detection well agree with the ones from $F-\delta$ curves as shown in Table 4.2. It is also noted that Ni-diamond nanocomposites with the average particle-diameter of 350 nm and 50 nm can have about 4.6% and 13.6% Young's modulus enhancement than that of pure electroplated Ni, respectively.

4.4.3 Fatigue Test

As aforementioned in Section 4.2 and Figure 4.1, the fatigue test is performed on microsized cantilever-beam specimens made of electroplated Ni and Ni-diamond nanocomposites using a micro-probe controlled by the test machine to cyclically apply a sinusoidal displacement (i.e. zero-tension loading) on the free end of tested beam with a frequency of 20 Hz. All of the fatigue testes are conducted in air and at room temperature. The fatigue lifetime is obtained from different cyclic displacement loadings which are

below δ_{max} for each fatigue test condition. As shown in Figure 4.6, the fatigue test results are performed in terms of $S-N$ curves. The $S-N$ curve, a plot of loading stress (S) versus the number of cycles to fracture (N) is generally utilized for presenting fatigue data. In this study, values of the loading stress (i.e. maximum stress) used in the $S-N$ curve are evaluated by FEA [15, 75, 76] from the cyclic displacement loading as shown in Figure 4.7 at the root corner with the maximum stress. In the $S-N$ curves of Figure 4.6, each data point is determined when the specimen is broken as shown in Figure 4.8, where the loading force detected by the load cell will become diminutive and the number of cycles to fracture will be recorded, simultaneously. In general, fatigue strength is defined as a stress value where the specimen has no failure after 10^6 cycles [66]. With the test frequency of 20 Hz, it takes about 14 hours for one specimen to run 10^6 cycles. From Figure 4.6, the fatigue strengths are found to be 2.41 GPa, 2.18 GPa, and 2.40 GPa of the electroplated Ni and Ni-diamond nanocomposites with the average particle-diameter of 350 nm and 50 nm, respectively. In addition, the derived fatigue strength of electroplated Ni film is a little higher than that of electroless Ni film (~1.89 GPa [76]). In Figure 4.6, it is also noted that the fatigue strength of Ni-diamond nanocomposite can have 10% increase with the reduction of nano-diamond particle size from 350 nm to 50 nm, and the fatigue lifetime of Ni-diamond nanocomposite with the average particle-diameter of 50 nm would be the same as that of pure electroplated Ni in the low stress cycling regime.

4.5 Discussions

Fatigue of ductile material is generally attributed to cyclic plastic deformation involving dislocation motion. The motion would result in the alternating, blunting, re-sharpening, and advancing of a crack tip in a material [77]. From the FEA calculated stress-distribution as shown in Figure 4.7, it can be found that the maximum stress value is

concentrated at two root corners of cantilever beam. Under cyclic stress loading, crack tip will occur initially at the stress-concentrated zone, such as the root corners of specimen, as shown in Figure 4.9(a). Then, the cracks will grow from these root corners of specimen (Figure 4.9(b)). Finally, the beam will fracture as soon as cracks from two ends meet together (Figure 4.9(c)). Figure 4.10 shows the SEM pictures of fatigue fracture interface of Ni-based beams; the cup-cone fracture morphology is a typical ductile characteristic of metal-based material.

In the foregoing Figure 4.6, it has shown that electroplated Ni-diamond nanocomposites have slightly smaller fatigue lifetime than that of pure electroplated Ni especially for large-size particles, which can be attributed to the ductility reduction by the incorporation of second-phase particles. As shown in Figures 4.10(a) and 4.10(b), due to the incorporation of second-phase particles, the cup-cone fracture morphology in Ni-diamond nanocomposite with the average particle-diameter of 350 nm is finer than the pure electroplated Ni one, and the fracture morphology becomes towards brittle fracture. In the nanocomposite system, nano-diamond particle is a source to generate dislocation but also a barrier to block dislocation motion because of the high hardness of diamond. Due to aggravated multiplication and motion hindrance of dislocations in the composite system, crack and void would be easily formed and make the material become brittle. Thus, both the fatigue lifetime and strength of Ni-diamond nanocomposite will degrade and become worse than that of pure electroplated Ni.

As aforementioned in Section 4.4.2, the electroplated Ni-diamond nanocomposites have higher Young's modulus values than that of pure electroplated Ni. Such improvement can be attributed to the particle reinforcement in matrix that the diamond has a larger Young's modulus (~1100 GPa [78]) than that of pure electroplated Ni (~156.7 GPa as measured). According to the rule-of-mixtures [21, 79], the Young's modulus of the

composite could be estimated as the one just falling between the upper and lower bounds as follows:

Upper bound based on the assumption that two phases in a composite are arranged in parallel,

$$E_{c,\text{parallel}} = E_m V_m + E_p V_p \tag{4.2}$$

and lower bound based on the assumption of two in-series phases,

$$E_{c,\text{series}} = \frac{E_m E_p}{E_m V_p + E_p V_m} \tag{4.3}$$

where E and V denote the Young's modulus and volume fraction, respectively, and the subscripts of c, m, and p represent composite, matrix, and particle phases. From Equations 4.2 and 4.3, the calculated upper and lower bound values of Young's moduli are 160.0 GPa and 157.2 GPa for the electroplated Ni-diamond nanocomposite with the average particle-diameter of 350 nm, and 160.6 GPa and 157.3 GPa for the one with the average particle-diameter of 50 nm, respectively. Therefore, based on the rule-of-mixtures, electroplated Ni-diamond nanocomposites can be explained to have higher Young's moduli than that of pure electroplated Ni. However, it is also noted that the calculated upper bound values of Young's moduli are lower than that listed in Table 4.2, especially for the small particle size. This can be found that the Young's modulus of nanocomposite depends on not only volume fraction of particle but also particle size.

Previously, there were few literatures to report particle size effect on fatigue lifetime in a composite system, and only focused on the micro-scale particle [80, 81]. For the composite material (Al/SiC_p) consolidated via powder metallurgy processing [80], the decrease of particle size from 25 μm to 5 μm was found to gain the strengthening and hardening effects which also resulted in the increases of fatigue lifetime and strength. In our proposed electroplated composite system with nanoparticles, under the same volume

fraction, more and more nanoparticles would be introduced into the electroplated composite system with a decrease in the particle size of the secondary phase. This could complicate the grain boundary system of the composite with different sliding systems which would hinder dislocation motion, make structure hardened, and prevent crack growth. Furthermore, small particle size means dislocations could still cut through or bypass the secondary phase under low cyclic loading. The cutting through or by-passing behavior would make the fracture behave more ductile even though the secondary phase could effectively result in the multiplication and motion hindrance of dislocations. Therefore, the fatigue lifetime and strength of the electroplated Ni-diamond nanocomposite can be improved by incorporating small-size particles as shown in Figure 4.6. In fact, the tendency has also been found in the fracture interfaces as shown in Figures 4.10(a) and 4.10(c), the cup-cone fracture morphology of Ni-diamond nanocomposite with the average particle-diameter of 50 nm appears closely to that of pure electroplated Ni.

4.6 Summery

Fatigue behavior of electroplated Ni and Ni-diamond nanocomposite including Young's modulus, fatigue lifetime, and fatigue strength, have been characterized by employing bending test on microsized cantilever-beam specimens. Experimental results show that Ni-diamond nanocomposite has higher Young's modulus than that of pure electroplated Ni due to the particle reinforcement in matrix, but it has slightly shorter fatigue lifetime and weaker fatigue strength than that of pure electroplated Ni due to the ductility reduction resulted by the nano-diamonds. Nevertheless, once incorporated diamond particle size is reduced from 350 nm to 50 nm, the fatigue lifetime of Ni-diamond nanocomposite can be improved and its fatigue strength can be as strong as the pure electroplated Ni. These improvements of fatigue lifetime and strength can be attributed to

the particle size effect. Under the same weight fraction, small diamond size means more diamond particles to complicate the composite grain boundary system which will hinder dislocation motion, make structure hardened, and prevent crack growth. Experimental data presented here would be helpful in considering fatigue issue while designing MEMS devices containing electroplated Ni film or Ni-diamond nanocomposite.

Table 4.1 Plating bath conditions of Ni-based materials for microsized cantilever-beam specimens.

Ni	
DC plating bath:	
Nickel sulfamate (g/L)	400
Nickel chloride (g/L)	5
Boric acid (g/L)	40
Wetting agent (c.c.)	5
pH	4.1 ~ 4.3
Current density (mA/cm^2)	10
Temperature (°C)	50
Ni-diamond nanocomposites	
DC plating bath:	
Nickel sulfamate (g/L)	400
Nickel chloride (g/L)	5
Boric acid (g/L)	40
Wetting agent (c.c.)	5
Concentration of diamond nanoparticles (g/L)	2
Average diameter of diamond nanoparticles (nm)	50, 350
pH	4.1 ~ 4.3
Current density (mA/cm^2)	10
Temperature (°C)	50

Table 4.2 Young's moduli of electroplated Ni and Ni-diamond nanocomposites derived from $F-\delta$ curves, nanoindenter measurement, and resonant frequency detection.

	Young's modulus (GPa)		
	$F-\delta$ curves	**Nanoindenter measurement**	**Resonant frequency detection**
Ni	156.9	156.7 ±5	158.1 ±2
Ni-diamond (avg. dia. 350 nm)	165.9	164.0 ±5	163.3 ±2
Ni-diamond (avg. dia. 50 nm)	178.2	178.0 ±5	178.2 ±2

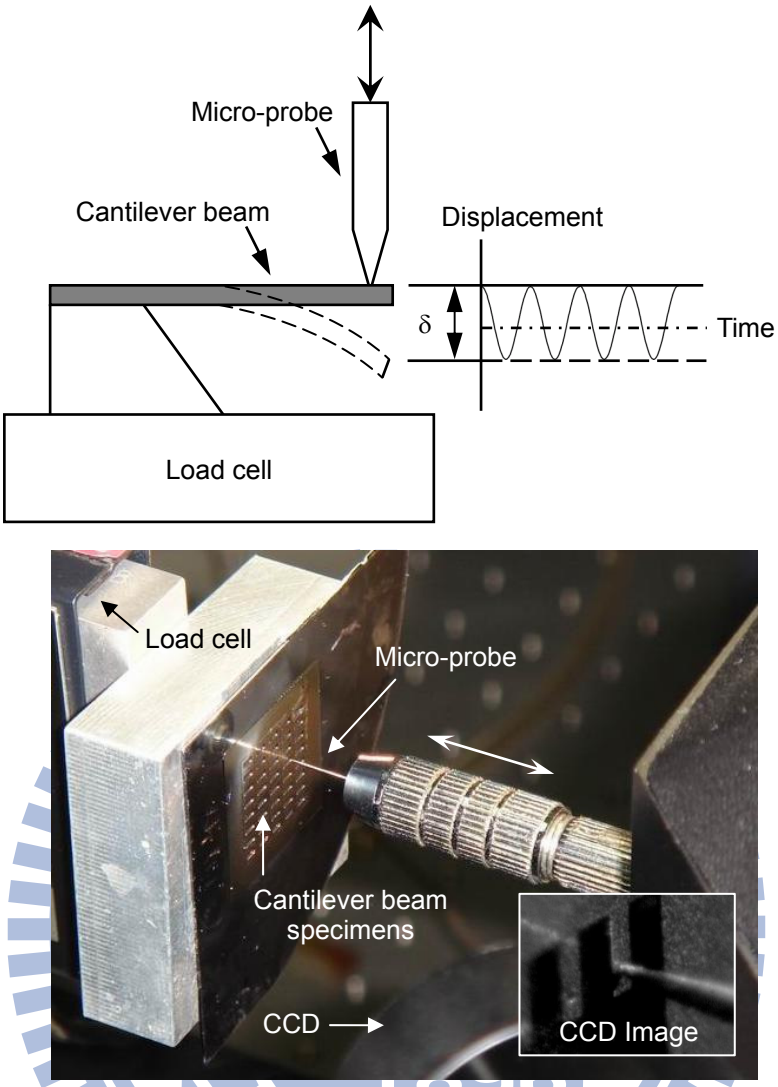

Figure 4.1 Set-up photo and schematic diagram of the bending-fatigue test for microsized cantilever-beam specimen.

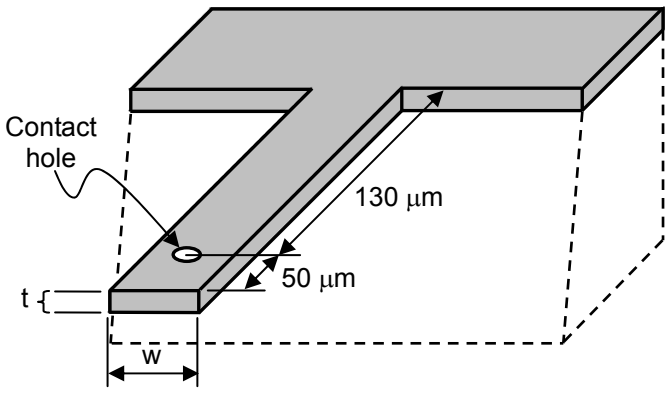

Figure 4.2 Illustration of microsized cantilever-beam specimen.

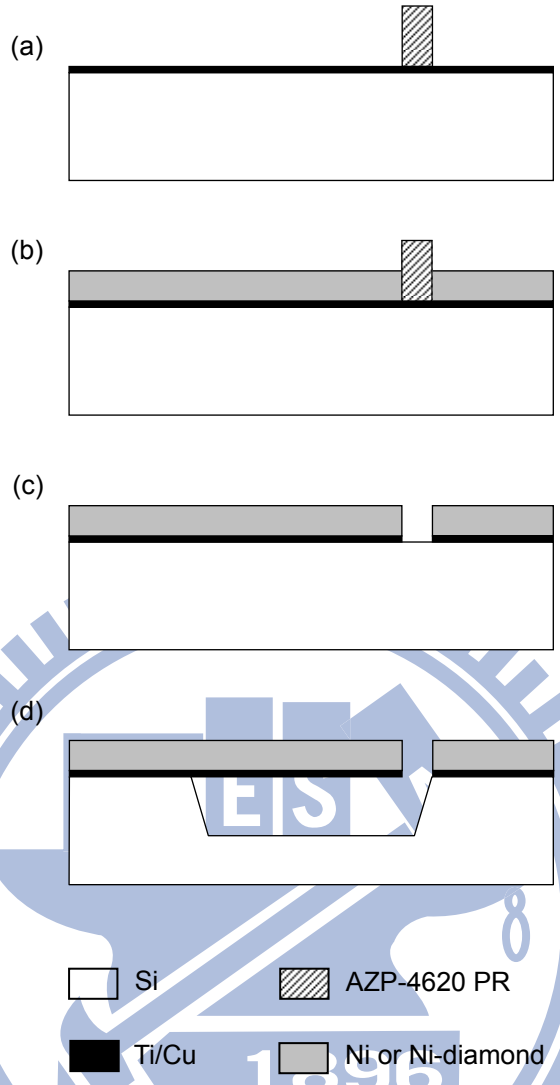

Figure 4.3 Fabrication process of microsized cantilever-beam specimen: (a) sputtered 200 Å Ti and 1000 Å Cu as an adhesion and seed layer on the cleaned silicon wafer, then coated and patterned 20 μm AZP-4620 PR as the plating mold; (b) electro-deposition of Ni-based material; (c) electroplated structure releasing; (d) silicon removing by KOH.

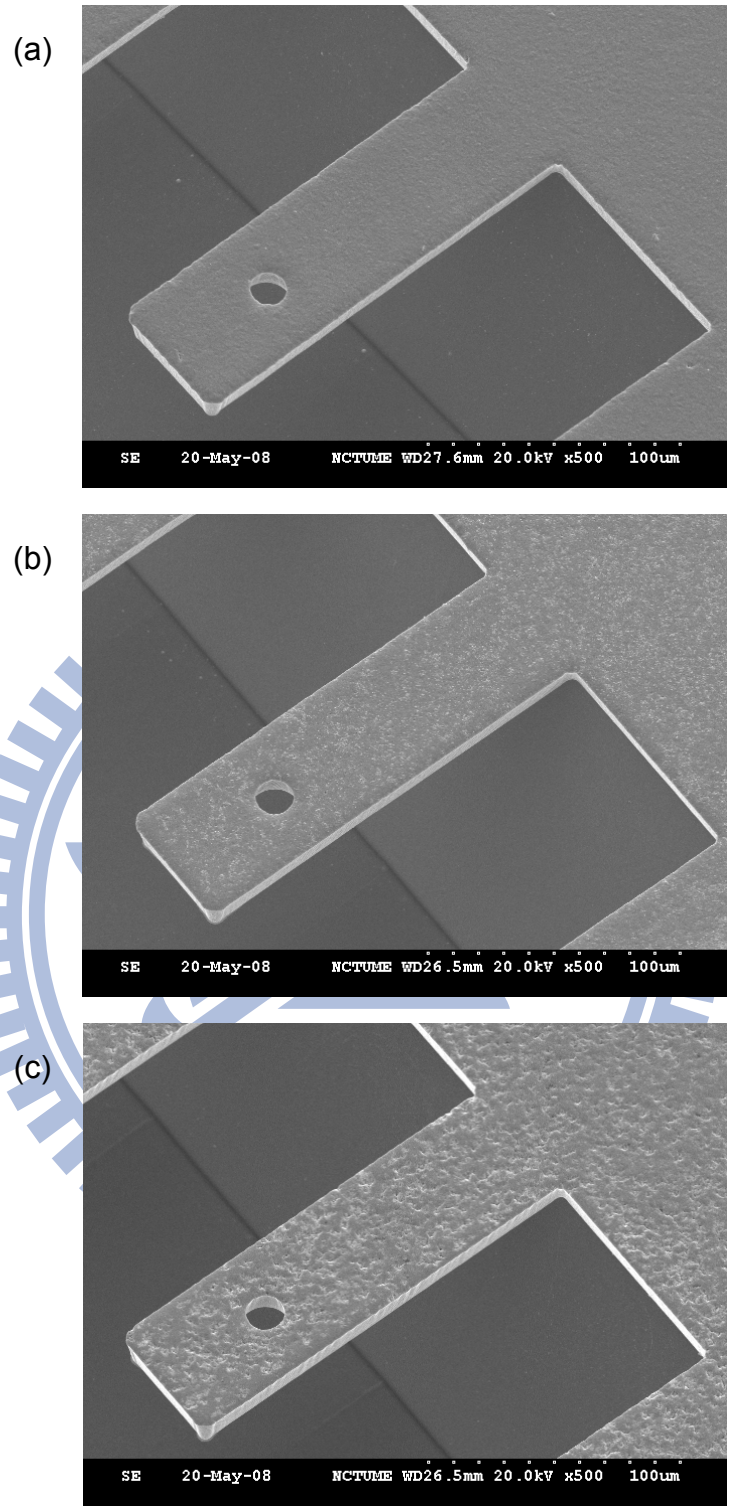

Figure 4.4 SEM pictures of as-electroplated cantilever-beam specimens made of: (a) Ni; (b) Ni-diamond nanocomposite with average particle-diameter of 350 nm; (c) Ni-diamond nanocomposite with average particle-diameter of 50 nm.

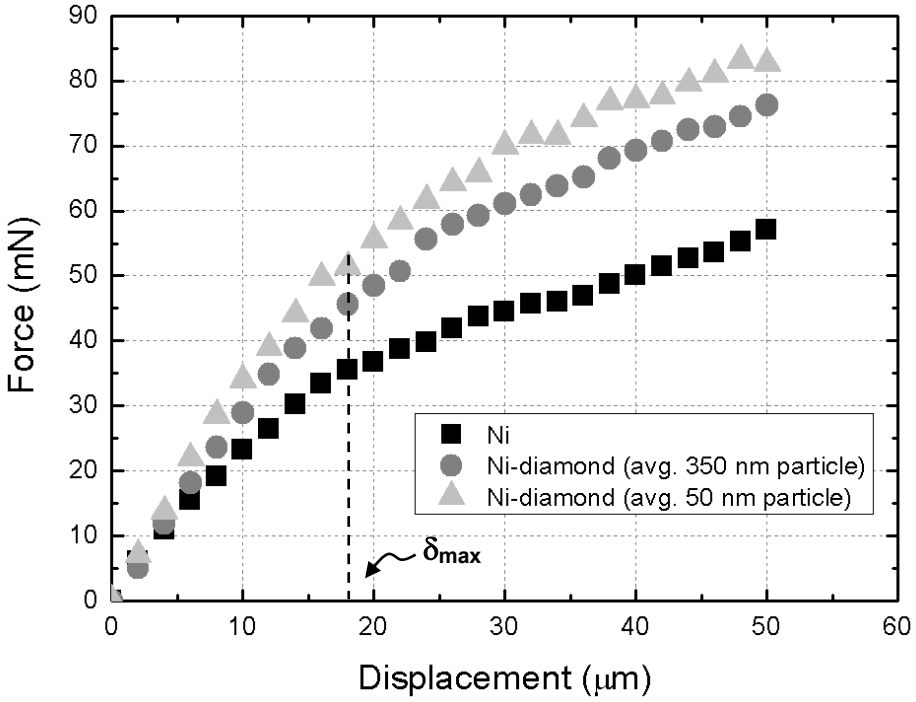

Figure 4.5 $F-\delta$ curves of microsized cantilever-beam specimens made of electroplated Ni and Ni-diamond nanocomposites from static bending tests.

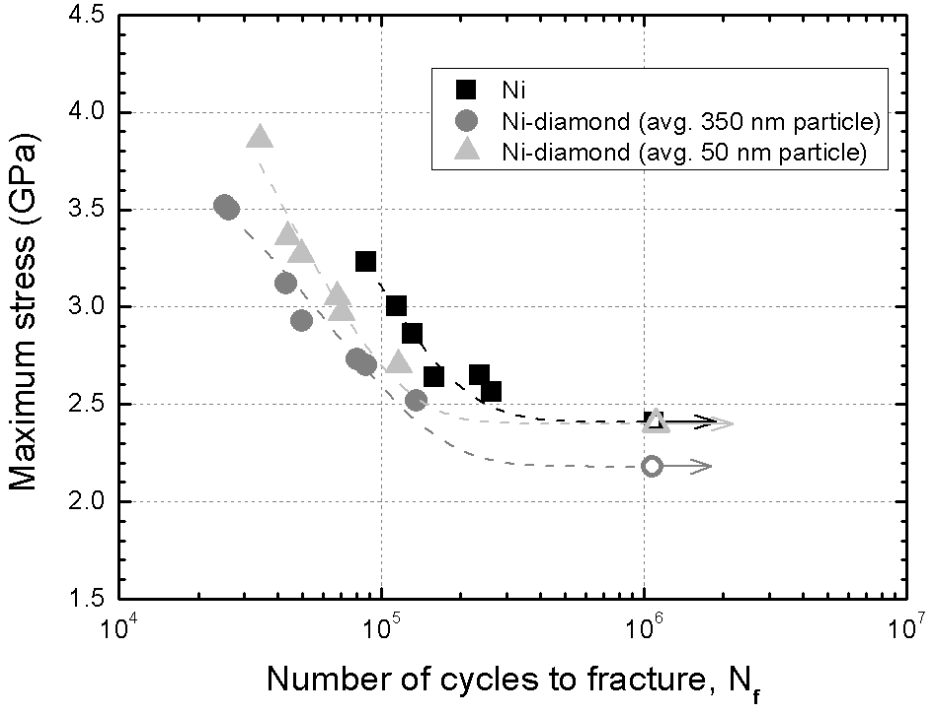

Figure 4.6 $S-N$ curves of microsized cantilever-beam specimens made of electroplated Ni and Ni-diamond nanocomposites from fatigue tests.

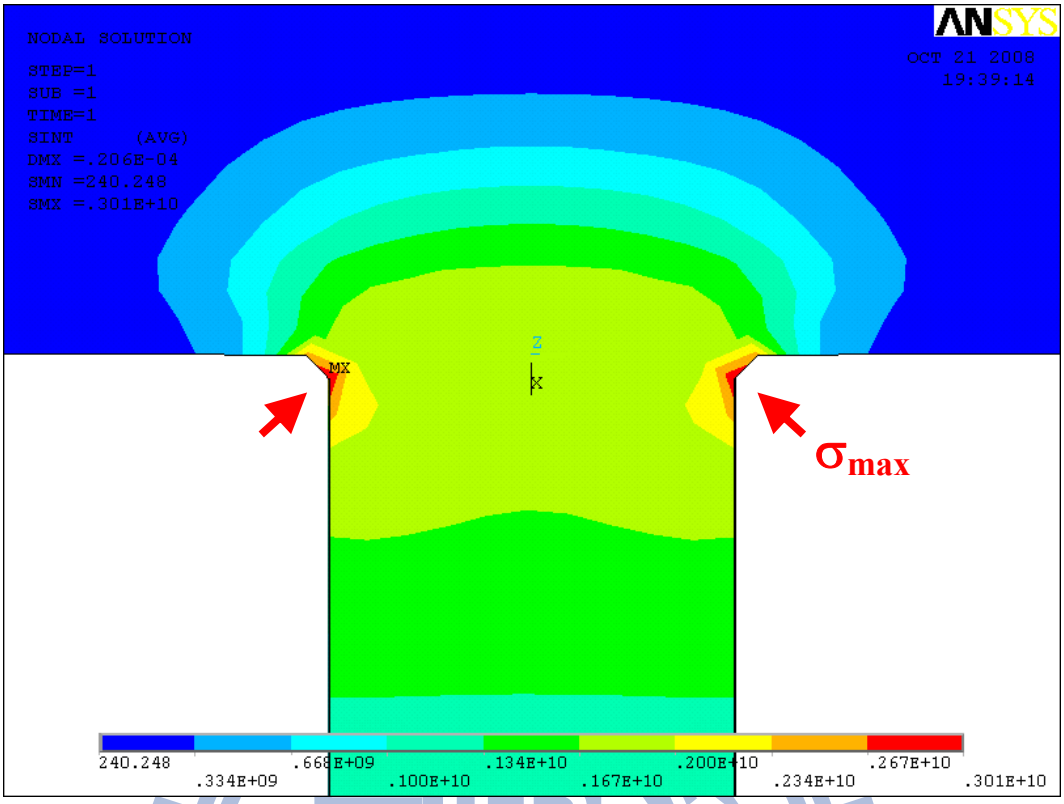

Figure 4.7 FEA calculated stress-distribution of specimen under the cyclic displacement loading.

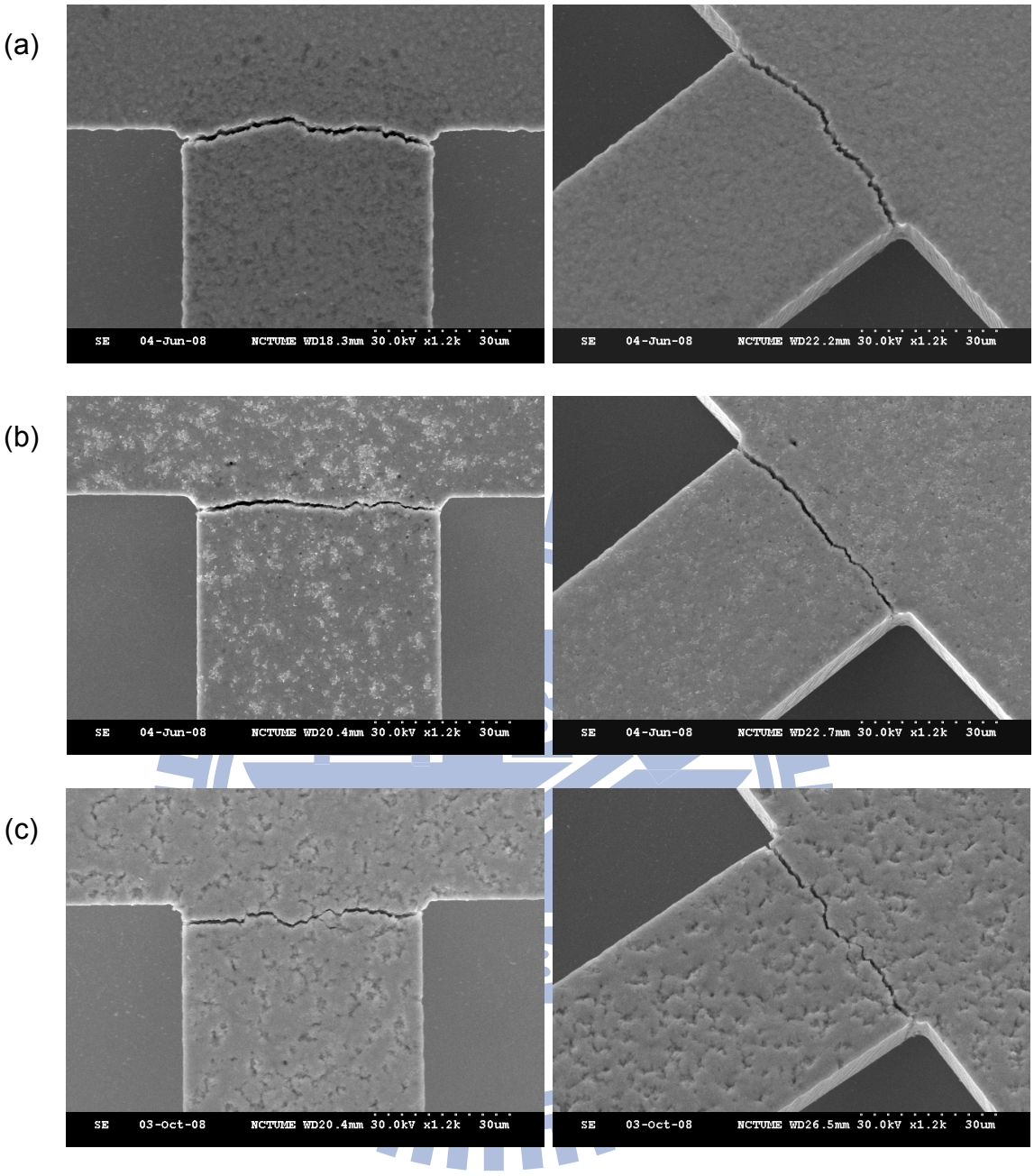

Figure 4.8 SEM pictures of electroplated specimen appearance after fatigue fracture: (a) Ni; (b) Ni-diamond nanocomposite with average particle-diameter of 350 nm; (c) Ni-diamond nanocomposite with average particle-diameter of 50 nm.

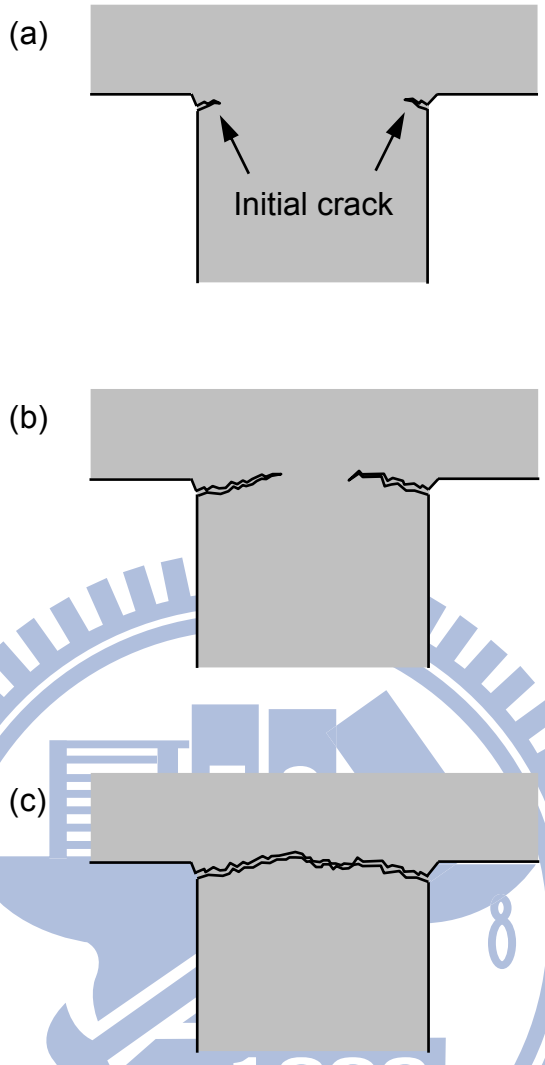

Figure 4.9 Schematic process of fatigue fracture on microsized cantilever-beam specimen: (a) crack initiation; (b) crack growth; (c) specimen failure.

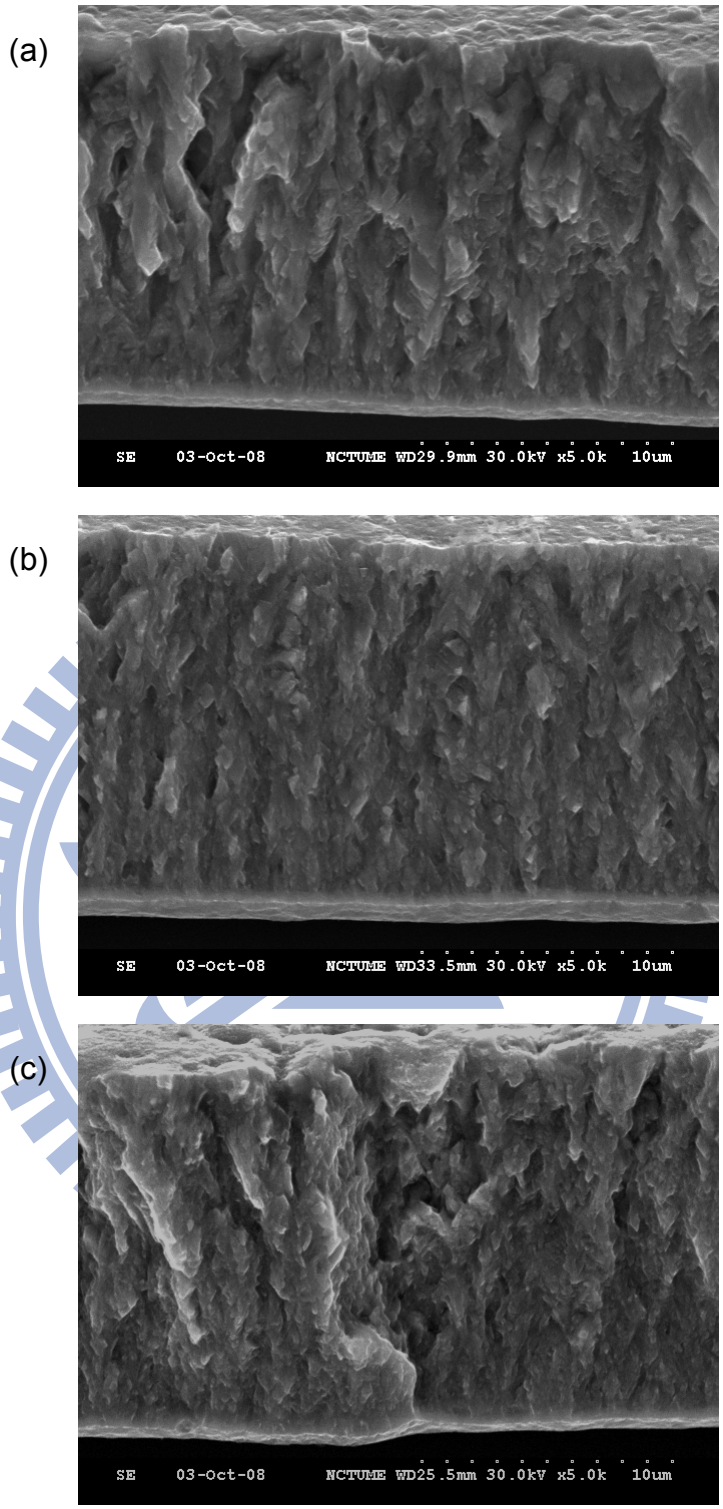

Figure 4.10 SEM pictures of cross-sectional morphology of electroplated specimen after fatigue test: (a) Ni; (b) Ni-diamond nanocomposite with average particle-diameter of 350 nm; (c) Ni-diamond nanocomposite with average particle-diameter of 50 nm.

Chapter 5 Conclusion

5.1 Summary

In this dissertation, CTE and fatigue properties of electroplated Ni-diamond nanocomposite have been investigated and characterized thoroughly in terms of CTE variation mechanism, material application, and reliability issue.

In Chapter 2, the promising mechanism of CTE enhancement and diminution in Ni-based nanocomposites can be attributed to the residual stress types resulted from co-electrodeposited process due to the differences of hardness or Young's modulus between matrix and particle reinforcement. Through the investigation on the diffraction peak shift from XRD pattern, the residual stress types of Ni-based nanocomposites can be determined comparing with the pure electroplated Ni matrix. According to the measurement results, Ni-diamond nanocomposite with residual compressive stress is observed to have higher CTE value than that of pure electroplated Ni; oppositely, Ni-SiO_2 nanocomposite with residual tensile stress is observed to have lower CTE value than that of pure electroplated Ni.

In Chapter 3, Ni-diamond nanocomposite is applied on the structural material of thermal bimaterial structure employing its CTE property for bimorph effect. Thermal bimaterial structure made of electroplated Ni and Ni-diamond nanocomposite shows better interfacial bonding strength and smaller residual thermal stress since Ni and Ni-diamond nanocomposite have different CTE but similar crystal structure and process temperature. Furthermore, by controlling the plating sequence of Ni and Ni-diamond nanocomposite, the fabricated thermal bimaterial structure desired to have upward or downward bended deformation can also be easily achieved.

In Chapter 4, the reliability issue and material property have been studied and characterized in terms of Young's modulus, fatigue lifetime, fatigue strength, and fracture behavior employing the bending-test method on microsized cantilever-beam specimens made of electroplated Ni and Ni-diamond nanocomposites with different particle sizes (i.e. 350 nm and 50 nm in diameter). The experimental results show that electroplated Ni-diamond nanocomposite has slightly smaller fatigue strength than that of pure electroplated Ni due to the ductility reduction resulted by the nano-diamond particles. However, once the incorporated particle size of nano-diamond is reduced from 350 nm to 50 nm, it has been found that the electroplated Ni-diamond nanocomposite can have higher Young's modulus and comparable fatigue strength with that of pure electroplated Ni. These improvements of fatigue lifetime and strength can be attributed to the particle size effect. In other words, under the same weight fraction, small diamond size means more diamond particles to complicate the composite grain boundary system which will hinder dislocation motion, make structure hardened, and prevent crack growth. Furthermore, these experimental data would be helpful in considering fatigue issue while designing MEMS devices containing electroplated Ni film or Ni-diamond nanocomposite.

From above thorough studies, Ni-diamond nanocomposite based on the electro-deposition technique has been thought undoubtedly as a suitable and potential structure material for further applications on micromachines and MEMS devices. In material properties, electroplated Ni-diamond nanocomposite has advantages of well wear resistance, high hardness, high Young's modulus, high CTE, stress-free, and comparable fatigue strength than that of pure electroplated Ni. In fabrication processes, electroplated Ni-diamond nanocomposite, like pure electroplated Ni with MEMS and CMOS compatibility, has advantages of one-step process, selective on-chip deposition, high deposition rate, low process temperature, and wafer-level fabrication.

5.2 Future Research Direction

The future research directions focus on CTE model derivation and extending application on MEMS-last. Although the residual stress types have be observed as the promising mechanism of CTE variation on Ni-based nanocomposites, a powerful CTE model is still a lack of this region needing to be derived in the future research. Furthermore, combing the foregoing advantages of material properties and fabrication processes, the electroplated Ni-diamond nanocomposite is expected to integrate CMOS for extending application in the future research.

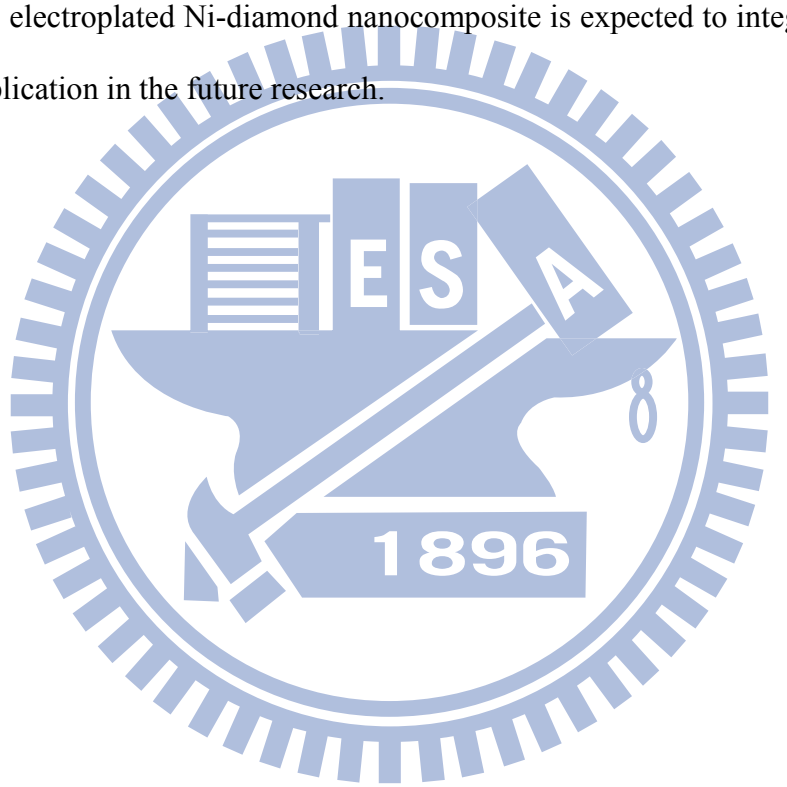

Reference

1. W. Ehrfeld, F. Götze, D. Münchmeyer, W. Schelb, and D. Schmidt, "LIGA process: Sensor construction techniques via X-ray lithography," *Proceedings of the IEEE Solid-State Sensor and Actuator Workshop*, Hilton Head, South Carolina, USA, pp. 1-4, 1988.
2. S. Furukawa, S. Roy, H. Miyajima, Y. Uenishi, and M. Mehregany, "Nickel surface micromachining," *Proceedings of the IEEE Microstructures and Microfabricated Systems*, San Francisco, California, USA, pp. 38-46, 1994.
3. P.M. Zavracky, S. Majumber, and E. McGruer, "Micromechanical switches fabricated using nickel surface micromachining," *J. Microelectromech. Syst.*, vol. 6, pp. 3-9, 1997.
4. C.P. Hsu, W.C. Tai, and W. Hsu, "Design and analysis of an electrothermally driven long-stretch micro drive with cascaded structure," *Proceedings of the ASME International Mechanical Engineering Congress & Exposition*, New Orleans, Louisiana, USA, 2002.
5. K. Kataoka, S. Kawamura, T. Itoh, K. Ishikawa, H. Honma, and T. Suga, "Electroplating Ni microcantilevers for low contact-force IC probing," *Sens. Actuators A*, vol. 103, pp. 116-121, 2003.
6. W.L. Huang, Z. Ren, Y.W. Lin, H.Y. Chen, J. Lahann, and C.T.C. Nguyen, "Fully monolithic CMOS nickel micromechanical resonator oscillator," *Proceeding of IEEE International Conference on Micro Electro Mechanical Systems*, Tucson, Arizona, USA, pp. 10-13, 2008.
7. C.T.J. Low, R.G.A. Wills, and F.C. Walsh, "Electrodeposition of composite coatings containing nanoparticles in a metal deposit," *Surf. Coat. Tech.*, vol. 201, pp. 371-383,

2006.

8. U. Erb, “Electrodeposited nanocrystals: synthesis, properties and industrial applications,” *Nanostruct. Mater.*, vol. 6, pp. 533-538, 1995.
9. A.F. Zimmermann, G. Palumbo, K.T. Aust, and U. Erb, “Mechanical properties of nickel silicon carbide nanocomposites,” *Mater. Sci. Eng. A*, vol. 328, pp. 137-146, 2002.
10. S. Zhang, D. Sun, Y. Fu, and H. Du, “Recent advances of superhard nanocomposite coatings: a review,” *Surf. Coat. Technol.*, vol. 167, pp. 113-119, 2003.
11. S. Neralla, D. Kumar, S. Yarmolenko, and J. Sankar, “Mechanical properties of nanocomposite metal-ceramic thin films,” *Composites B*, vol. 35, pp. 157-162, 2004.
12. L.N. Tsai, G.R. Shen, Y.T. Cheng, and W. Hsu, “Performance improvement of an electrothermal microactuator fabricated using Ni-diamond nanocomposite,” *J. Microelectromech. Syst.*, vol. 15, pp. 149-158, 2006.
13. L.N. Tsai, Y.T. Cheng, and W. Hsu, “Nanocomposite effects on the of thermal expansion modification for high performance electro-thermal microactuator,” *Proceeding of IEEE International Conference on Micro Electro Mechanical Systems*, Miami, Florida, USA, pp. 467-470, 2005.
14. Y.C. Lee, L.N. Tsai, Y.T. Cheng, and W. Hsu, “Performance enhancement of comb drive actuators utilizing electroplated nickel-diamond nanocomposite,” *Proceedings of the Asia-Pacific Conference on Transducers and Micro-Nano Technology*, Singapore, 2006.
15. K.P. Larsen, A.A. Rasmussen, J.T. Ravnkilde, M. Ginnerup, and O. Hansen, “MEMS device for bending test measurements of fatigue and creep of electroplated nickel,” *Sens. Actuators A*, vol. 103, pp. 156-164, 2003.
16. Metal Matrix Composites (http://www.cmt-ltd.com/html/mat_1.htm).

17. J. Zahavi and J. Hazan, “Electrodeposited nickel composites containing diamond particles,” *Plat. Surf. Finish.*, vol. 70, pp. 57-61, 1983.

18. W.H. Lee, S.C. Tang, K.C. Chung, “Effects of direct current and pulse-plating on the co-deposition of nickel and nanometer diamond powder,” *Surf. Coat. Tech*, vol. 120-121, pp. 607-611, 1999.

19. E.C. Lee and J.W. Choi, “A study on the mechanism of formation of electrocodeposited Ni-diamond coatings,” *Surf. Coat. Tech.*, vol. 148, pp. 234-240, 2001.

20. K.S. Teh, Y.T. Cheng, and L. Lin, “MEMS fabrication based on nickel-nanocomposite: film deposition and characterization,” *J. Micromech. Microeng.*, vol. 15, pp. 2205-2215, 2005.

21. W.D. Callister Jr., *Materials Science and Engineering an Introduction*, Wiley, New York, 4th ed., 1996.

22. H.S. Cho, K.J. Hemker, K. Kian, J. Goettert, and G. Dirras, “Measured mechanical properties of LIGA Ni structures,” *Sens. Actuators A*, vol. 103, pp. 59-63, 2003.

23. D. Son, J. Kim, T.W. Lim, and D. Kwon, “Evaluation of fatigue strength of LIGA nickel film by microtensile tests,” *Scr. Mater.*, vol. 50, pp. 1265-1269, 2004.

24. Y. Yang, B.I. Imasogie, S.M. Allameh, B. Boyce, K. Lian, J. Lou, and W.O. Soboyejo, “Mechanisms of fatigue in LIGA Ni MEMS thin films,” *Mat. Sci. Eng. A*, vol. 444, pp. 39-50, 2007.

25. S. Maekawa, K. Takashima, M. Shimojo, Y. Higo, S. Sugiura, B. Pfister, and M.V. Swain, “Fatigue tests of Ni-P amorphous alloy microcantilever beams,” *Jpn. J. Appl. Phys.*, vol. 38, pp. 7194-7198, 1999.

26. A.A. Fahmy and A.N. Ragai, “Thermal-expansion behavior of two-phase solids,” *J. Appl. Phys.*, vol. 41, pp. 5108-5111, 1970.

27. H.A. Bruck and B.H. Rabin, “Evaluation of rule of mixtures predictions of thermal expansion in powder-processed Ni-Al_2O_3 composite,” *J. Am. Ceram. Soc.*, vol. 82, pp. 2927-2930, 1999.
28. S. Lemieux and S. Elomari, “Thermal expansion of isotropic duralcan metal-matrix composites,” *J. Mater. Sci.*, vol. 33, pp. 4381-4387, 1998.
29. P.S. Turner, “Thermal-expansion stresses in reinforced plastics,” *J. Res. Nat. Bur. Std.*, vol. 37, pp. 239, 1946.
30. E.H. Kerner, “The elastic and thermo-elastic properties of composite media,” *Proceedings of the Physical Society Section B*, vol. 69, pp. 808-813, 1956.
31. R.A. Schapery, “Thermal expansion coefficients of composite materials based on energy principles,” *J. Compos. Mater.*, vol. 2, pp. 380-404, 1968.
32. Z. Hashin and S. Shtrikman, “A variational approach to the theory of the elastic behavior of multiphase materials,” *J. Mech. Phys. Solids*, vol. 11, pp. 127-134, 1963.
33. P. Hess, “Laser diagnostics of mechanical and elastic properties of silicon and carbon films,” *Appl. Surf. Sci.*, vol. 106, pp. 429-437, 1996.
34. R. Birringer, “Nanocrystalline materials,” *Mat. Sci. Eng. A*, vol. 117, pp. 33-43, 1989.
35. K. Lu and M.L. Sui, “Thermal expansion behaviors in nanocrystalline materials with a wide grain size range,” *Acta metall. mater.*, vol. 43, pp. 3325-3332, 1995.
36. L.H. Qian, S.C. Wang, Y.H. Zhao, and K. Lu, “Microstrain effect on thermal properties of nanocrystalline Cu,” *Acta Mater.*, vol. 50, pp. 3425-3434, 2002.
37. I.W. Gazda, “Variations in CTE as function of prestressing,” *Carbon*, vol. 8, pp. 511-515, 1970.
38. P.E. Hart, “The effect of pre-stressing on the thermal expansion and Young’s modulus of graphite,” *Carbon*, vol. 10, pp. 233-236, 1971.
39. W. Fang and C.Y. Lo, “On the thermal expansion coefficients of thin films,” *Sens.*

Actuators A, vol. 84, pp. 310-314, 2000.

40. O.D Slagle, "Thermal expansion hysteresis in polycrystalline graphite," *Carbon*, vol. 7, pp. 337-344, 1969.
41. B.D. Cullity and S.R. Stock, *Elements of X-ray diffraction*, Prentice Hall, New Jersey, 3rd ed., pp. 167-177, 2001.
42. B.B. Panigrahi and M.M. Godkhindi, "Structural changes and thermal expansion behavior of ultrafine titanium powders during compaction and heating," *J. Mater. Res.*, vol. 20, pp. 580-585, 2005.
43. K. Tanaka and Y. Akiniwa, "Diffraction measurements of residual macrostress and microstress using X-rays, synchrotron and neutrons," *JSME Int. J. Ser. A*, vol. 47, pp. 252-263, 2004.
44. T. Namazu and S. Inoue, "Characterization of single crystal silicon and electroplated nickel films by uniaxial tensile test with in situ X-ray diffraction measurement," *Fatigue Fract. Engng. Mater. Struct.*, vol. 30, pp. 13-20, 2006.
45. W.H. Chu, M. Mehregany, and R.L. Mullen, "Analysis of tip deflection and force of a bimorph cantilever microactuator," *J. Micromech. Microeng.*, vol. 3, pp. 4-7, 1993.
46. H. Sehr, A.G.R. Evans, A. Brunnschweiler, G.J. Ensell, and T.E.G. Niblock, "Fabrication and test of thermal vertical bimorph actuators for movement in the wafer plane," *J. Micromech. Microeng.*, vol. 11, pp. 306-310, 2001.
47. S.H. Lim, J. Choi, R. Horowitz, and A. Majumdar, "Design and fabrication of a novel bimorph microoptomechanical sensor," *J. Microelectromech. Syst.*, vol. 14, pp. 683-690, 2005.
48. W. Fang and J.A. Wickert, "Comments on measuring thin-film stress using bi-layer micromachined beams," *J. Micromech. Microeng.*, vol. 5, pp. 276-281, 1995.
49. M.Y. Al Aioubi, V. Djakov, S.E. Huq, and P.D. Prewett, "Deflection and load

characterisation of bimorph actuators for bioMEMS and other applications," *Microelectron. Eng.*, vol. 73–74, pp. 898-903, 2004.

50. H. Jerman, "Electrically activated normally closed diaphragm valves," *J. Micromech. Microeng.*, vol. 4, pp. 210-216, 1994.
51. C. Hsu and W. Hsu, "A two-way membrane-type micro-actuator with continuous deflections," *J. Micromech. Microeng.*, vol. 10, pp. 387-394, 2000.
52. S. Schweizer, S. Calmes, M. Laudon, and P. Renaud, "Thermally actuated optical microscanner with large angle and low consumption," *Sens. Actuators A*, vol. 76, pp. 470-477, 1999.
53. S. Zhou, X. Sun, and W.N. Carr, "A monolithic variable inductor network using microrelays with combined thermal and electrostatic actuation," *J. Micromech. Microeng.*, vol. 9, pp. 45-50, 1999.
54. W. Riethmuller and W. Benecke, "Thermally excited silicon microactuator," *IEEE Trans. Electron Devices*, vol. ED-35, pp. 758-763, 1988.
55. F. Spaepen and A.L. Shull, "Mechanical properties of thin films and multilayers," *Curr. Opin. Solid State Mater. Sci.*, vol. 1, pp. 679-683, 1996.
56. M.T.K. Hou and R. Chen, "Effect of width on the stress-induced bending of micromachined bilayer cantilevers," *J. Micromech. Microeng.*, vol. 13, pp. 141-148, 2003.
57. A. Jain, H. Qu, S. Todd, and H. Xie, "A thermal bimorph micromirror with large bi-directional and vertical actuation," *Sens. Actuators A*, vol. 122, pp. 9-15, 2005.
58. S.P. Baker, X. Wang, and C.Y. Hui, "Effect of nonlinear elastic behavior on bilayer decohesion of thin metal films from nonmetal substrates," *J. Appl. Mech.*, vol. 69, pp. 407-414, 2002.
59. C.A. Taylor, M.F. Wayne, and W.K.S. Chiu, "Heat treatment of thin carbon films and

the effect on residual stress, modulus, thermal expansion and microstructure," *Carbon*, vol. 41, pp.1867-1875, 2003.

60. Y.Q. Fu, H.J. Du, and S. Zhang, "Sputtering deposited TiNi films: relationship among processing, stress evolution and phase transformation behaviors," *Surf. Coat. Technol.*, vol. 167, pp. 120-128, 2003.
61. G. Lin, C.J. Kim, S. Konishi, and H. Fujita, "Design, fabrication, and testing of a C-shape actuator," *Proceedings of Transducers '95-Eurosensors IX*, Stockholm, Sweden, pp. 416-419, 1995.
62. Y. Zhang, Y. Zhang, and R.B. Marcus, "Thermally actuated microprobes for a new wafer probe card," *J. Microelectromech. Syst.*, vol. 8, pp. 43-49, 1999.
63. Anthony C. Fischer-Cripps, *Nanoindentation*, Springer, New York, 1st ed., pp. 27-30, 2002.
64. W. Peng, Z. Xiao, and K.R. Farmer, "Optimization of thermally actuated bimorph cantilevers for maximum deflection," *Nanotech*, vol. 1, pp. 376-379, 2003.
65. S.S. Kessler, S.M. Spearing, M.J. Atalla, C.E.S. Cesnik, and C. Soutis, "Damage detection in composite materials using frequency response methods," *Composites Part B*, vol. 33, pp. 87-95, 2002.
66. J.E. Shigley, C.R. Mischke, and R.G. Budynas, *Mechanical engineering design*, Mc Graw Hill, New York, 7th ed., pp. 313-315, 2003.
67. C.H. Lin, C.C. Yeh, C.P. Hsu, and W. Hsu, "Design and fabrication of a cascaded electro-thermal bimorph actuator," *Proceedings of the ASME International Mechanical Engineering Congress & Exposition*, Orlando, Florida, USA, 2005.
68. T. Yi and C.J. Kim, "Measurement of mechanical properties for MEMS materials," *Meas. Sci. Technol.*, vol. 10, pp. 706-16, 1999.
69. S. Johansson, J.Å. Schweitz, L. Tenerz, and J. Tirén, "Fracture testing of silicon

microelements in situ in a scanning electron microscope," *J. Appl. Phys.*, vol. 63, pp. 4799-4803, 1988.

70. H.K. Liu, B.J. Lee, and P.P. Liu, "Low cycle fatigue of single crystal silicon thin films," *Sens. Actuators A*, vol. 140, pp. 257-265, 2007.
71. C.J. Wilson, A. Ormeggi, and M. Narbutovskih, "Fracture testing of silicon microcantilever beams," *J. Appl. Phys.*, vol. 79, pp. 2386-2393, 1996.
72. R.R. Craig Jr., *Mechanics of material*, Wiley, New York, pp. 366, 1996.
73. C. Hsu, C. Tsou, and W. Fang, "Measuring thin film elastic modulus using a micromachined cantilever bending test by nanoindenter," *J. Micro/Nanolith. MEMS MOEMS*, vol. 6, pp. 033011, 2007.
74. L. Kiesewetter, J.M. Zhang, D. Houdeau, and A. Steckenborn, "Determination of Young's moduli of micromechanical thin films using the resonance method," *Sens. Actuators A*, vol. 35, pp. 153-159, 1992.
75. S.M. Allameh, P. Shrotriya, A. Butterwick, S.B. Brown, and W.O. Soboyejo, "Surface topography evolution and fatigue fracture in polysilicon MEMS structures," *J. Microelectromech. Syst.*, vol. 12, pp. 313-324, 2003.
76. S. Maekawa, K. Takashima, M. Shimojo, Y. Higo, S. Sugiura, B. Pfister, and M.V. Swain, "Fatigue tests of NI-P amorphous alloy microcantilever beams," *Proceedings of the International Conference on Microprocesses and Nanotechnology*, Yokohama, Japan, pp. 132-133, 1999.
77. C.L. Muhlstein, E.A. Stach, and R.O. Ritchie, "Mechanism of fatigue in micron-scale films of polycrystalline silicon for microelectromechanical systems," *Appl. Phys. Lett.*, vol. 80, pp. 1532-1534, 2002.
78. D. Schneider and M.D. Tucker, "Non-destructive characterization and evaluation of thin films by laser-induced ultrasonic surface waves," *Thin Solid Films*, vol. 290-291,

pp. 305-311, 1996

79. C.L. Hsieh and W.H. Tuan, “Elastic and thermal expansion behavior of two-phase composites,” *Mater. Sci. Eng. A*, vol. 425, pp. 349-360, 2006.

80. N. Chawla, C. Andres, J.W. Jones, and J.E. Allison, “Effect of SiC volume fraction and particle size on the fatigue resistance of a 2080 Al/SiC_p composite,” *Metall. Mater. Trans. A*, vol. 29, pp. 2843-2854, 1998.

81. Y. Uematsu, K. Tokaji, and M. Kawamura, “Fatigue behaviour of SiC-particulate-reinforced aluminium alloy composites with different particle sizes at elevated temperatures,” *Compos. Sci. Technol.*, vol. 68, pp. 2785-2791, 2008.

Publication List

- **Journal papers:**

1. Chia-Sheng Huang, Yu-Ting Cheng, Junwei Chung, and Wensyang Hsu, "Investigation of Ni-based thermal bimaterial structure for sensor and actuator application," *Sensors and Actuators A*, vol. 149, pp. 298-304, 2009.
2. Chia-Sheng Huang, Yu-Ting Cheng, Chang-Jhih Yeh, Hsien-Kuang Liu, and Wensyang Hsu "Characterization of fatigue behavior on electroplated Ni-diamond nanocomposites with different particle sizes," *Sensors and Actuators A*. (Submitted)

- **Conference papers:**

1. Chia-Sheng Huang, Yu-Ting Cheng, Chang-Jhih Yeh, Hsien-Kuang Liu, and Wensyang Hsu, "Young's modulus and fatigue lifetime improvements by diamond size effect on electroplated Ni-diamond nanocomposite," *Proceedings of the 15th International Conference on Solid-State Sensors, Actuators and Microsystems (IEEE Transducers 2009)*, Denver, U.S.A, pp. 180-183, 2009.
2. Chia-Sheng Huang, Junwei Chung, Yu-Ting Cheng, and Wensyang Hsu, "Thermal bimetallic microactuators by Ni and Ni-diamond nanocomposite," *Proceedings of the 2nd IEEE International Conference on Nano/Micro Engineered and Molecular Systems (IEEE NEMS)*, Bangkok, Thailand, pp. 37-40, 2007.
3. Yi-Chung Lo, Chia-Sheng Huang, Wensyang Hsu, Chaoen Wang, "Neural guidance by open-top SU-8 microfluidic channel," *Proceedings of IEEE International Conference on MEMS NANO and Smart System (IEEE-ICMENS)*, Alberta, Canada, pp. 671-674, 2004.